

1

2

3

4

# Cosmic ray validation of electrode positions in small-strip thin gap chambers for the upgrade of the ATLAS detector

5

Lia Formenti

6

7

8

Department of Physics  
McGill University, Montreal  
October, 2021

9

10

11

12

13

A thesis submitted to  
McGill University  
in partial fulfillment of the  
requirements of the degree of  
Master of Science

# <sup>15</sup> Table of Contents

<sup>16</sup>	<b>1</b>	<b>Introduction</b>	<b>1</b>
<sup>17</sup>	<b>2</b>	<b>High energy particle physics</b>	<b>4</b>
<sup>18</sup>	2.1	The Standard Model . . . . .	4
<sup>19</sup>	2.2	Beyond the Standard Model . . . . .	6
<sup>20</sup>	2.3	Studying high energy particle physics with accelerators . . . . .	7
<sup>21</sup>	<b>3</b>	<b>The LHC and the ATLAS experiment</b>	<b>9</b>
<sup>22</sup>	3.1	The Large Hadron Collider . . . . .	9
<sup>23</sup>	3.2	The High-Luminosity LHC . . . . .	10
<sup>24</sup>	3.3	The ATLAS experiment . . . . .	12
<sup>25</sup>	<b>4</b>	<b>The New Small Wheels</b>	<b>18</b>
<sup>26</sup>	4.1	Motivation for the New Small Wheels (NSWs) . . . . .	18
<sup>27</sup>	4.2	Design of the NSWs . . . . .	20
<sup>28</sup>	4.3	Small-strip thin gap chambers . . . . .	22
<sup>29</sup>	4.4	sTGC Quadruplet Construction . . . . .	23
<sup>30</sup>	4.5	NSW alignment . . . . .	26
<sup>31</sup>	<b>5</b>	<b>Using cosmic muons to measure relative strip position offsets</b>	<b>29</b>
<sup>32</sup>	5.1	Cosmic rays . . . . .	29
<sup>33</sup>	5.2	Experimental setup . . . . .	30

34	5.3 Data acquisition . . . . .	31
35	5.4 Data preparation . . . . .	31
36	5.4.1 Cuts on electrode hits . . . . .	31
37	5.4.2 Clustering and tracking . . . . .	32
38	5.5 Measuring relative local offsets . . . . .	34
39	5.6 Visualizing relative alignment between layers . . . . .	37
40	5.7 Systematic uncertainty . . . . .	39
41	5.8 Discussion . . . . .	41
42	<b>6 Using x-rays to measure relative strip position offsets</b>	<b>42</b>
43	6.1 Experimental setup . . . . .	42
44	6.2 Data acquisition . . . . .	44
45	6.3 Data preparation . . . . .	44
46	6.4 Measuring local offsets . . . . .	44
47	6.5 Measuring relative local offsets . . . . .	46
48	<b>7 Comparing cosmic muon and x-ray relative strip position offsets</b>	<b>50</b>
49	7.1 Assessing correlation . . . . .	50
50	7.2 Discussion . . . . .	55
51	<b>8 Outlook and summary</b>	<b>57</b>
52	8.1 Outlook . . . . .	57
53	8.2 Summary . . . . .	58
54	<b>References</b>	<b>59</b>
55	<b>APPENDICES</b>	<b>67</b>
56	<b>A Cluster position uncertainty</b>	<b>68</b>
57	A.1 Cluster definition . . . . .	68
58	A.2 Effect of fit algorithm on cluster mean . . . . .	68
59	A.3 Effect of uncertainty in cluster mean on track residuals . . . . .	69

60	<b>B Analysis statistics</b>	70
61	<b>C Analysis systematics</b>	72
62	C.1 Residual distribution fit function . . . . .	72
63	C.2 Cosmic muon data collection voltage . . . . .	73
64	C.3 Cluster fit algorithm . . . . .	75
65	C.4 Differential non-linearity . . . . .	76
66	<b>D Printable plots</b>	79

## Abstract

68 The Large Hadron Collider (LHC) is used to generate subatomic physics processes at the  
69 energy frontier to challenge our understanding of the Standard Model of particle physics.  
70 The particle collision rate at the LHC will be increased up to seven times its design value in  
71 2025-2027 by an extensive upgrade program. The innermost endcaps of the ATLAS muon  
72 spectrometer consist of two wheels of muon detectors that must be replaced to maintain  
73 the muon momentum resolution in the high-rate environment. The so-called New Small  
74 Wheels (NSWs) are made of two detector technologies: micromegas and small-strip thin gap  
75 chambers (sTGCs). The sTGCs are gas ionization chambers that hold a thin volume of gas  
76 between two cathode boards. One board is segmented into copper readout strips of 3.2 mm  
77 pitch that are used to precisely reconstruct the coordinate of a passing muon. Modules of  
78 four sTGCs glued together into quadruplets cover the NSWs. Quadruplets were designed  
79 to achieve a 1 mrad angular resolution to fulfill the spectrometer's triggering and precision  
80 tracking requirements. To achieve the required angular resolution the absolute position of  
81 the readout strips must be known in the ATLAS coordinate system to within 100  $\mu\text{m}$ . At  
82 McGill University, the performance of sTGC quadruplets was characterized using cosmic ray  
83 data before being sent to CERN, where the charge profile left by x-rays is used to measure  
84 the offset of the strip patterns with respect to nominal at a limited number of points on  
85 the surface of each quadruplet. The x-ray strip position measurements have acceptable but  
86 limited precision and do not span the whole area of the strip layers. Given the importance of  
87 knowing the absolute position of each readout strip to achieve the performance requirements  
88 of the NSWs, the x-ray method must be validated by an independent method. Cosmic ray  
89 data is used to characterize the relative alignment between layers and validate the x-ray  
90 method.

## Résumé

Le collisioneur LHC est utilisé pour générer des processus de la physique subatomique à la frontière d'énergie pour remettre en cause le modèle standard de la physique des particules. Le taux des collisions du collisioneur LHC augmentera jusqu'à sept fois le taux nominal en 2025-2027 par un programme d'amélioration majeur et varié. Une partie du spectromètre à muons est composée de deux roues de détecteurs de muons qu'il faut remplacer pour maintenir la résolution d'élan après l'augmentation du taux. Appelées les Nouvelles Petites Roues (NSWs), elles en utilisent deux technologies: des chambres micromegas et des chambres sTGCs (chambres à petites bandes et à intervalles fins). Les sTGCs sont des chambres d'ionisation de gaz, qui contiennent un volume de gaz fin entre deux panneaux cathodiques. Un panneau est segmenté à petites bandes en cuivre avec une pente de 3.2 mm qui se servent comme des voies de signal pour reconstruire précisément la coordonnée d'un muon qui passe. Des modules de quatre sTGCs collés ensemble en quadruplets couvrent les NSWs. Les quadruplets étaient conçus pour réaliser une résolution angulaire de 1 mrad pour satisfaire les exigences des systèmes de déclenchement et de mesures de précision. Pour réaliser la résolution angulaire il faut que la position absolue de chaque bande soit connue dans ATLAS avec une précision à moins de 100  $\mu\text{m}$ . À l'Université de McGill, la performance des quadruplets étaient caractériser avec des rayons cosmiques avant les envoyer à CERN, où le profil de charge laisser par des rayons-X est utilisé pour mesurer le déplacement du motif des bandes par rapport à nominal à un nombre de position limité sur la surface des quadruplets. Les déplacements mesurés pas les rayons-X ont une précision acceptable mais limitée, et ne couvrent pas la région entière des panneaux. Étant donné l'importance de savoir la position absolue de chaque bande pour réaliser les exigences de performance des NSWs, il faut une méthode indépendante pour valider la méthode des rayons-X. Les données recueillies avec les rayons cosmiques sont utilisées pour charactariser l'alignement relatif entre les panneaux et pour valider la méthode des rayons-X.

## Acknowledgements

- 118 Experimental particle physics projects are never done alone. I am grateful to have been  
119 working with the ATLAS Collaboration for two years now.
- 120 Thank you to Dr. Brigitte Vachon for her guidance throughout this project and for editing  
121 this thesis. I am consistently amazed by her ability to jump into the details of my project  
122 and discuss them with me.
- 123 Thanks also to Dr. Benoit Lefebvre, who collected some of the data used in this thesis, wrote  
124 several software tools I used to analyze the data and advised me several times throughout  
125 this project.
- 126 Thank you to my labmates at McGill University, Dr. Tony Kwan, Kathrin Brunner, John  
127 McGowan and Charlie Chen. Kathrin taught me mechanical skills that I will apply elsewhere.  
128 Tony, manager of the laboratory, created the most encouraging, trusting and productive work  
129 environment I have ever been apart of.
- 130 Thank you to the friends I can call on at anytime, and thank you to my family whose  
131 constant support makes every step possible.

## Contribution of authors

I, the author, was involved in collecting the cosmic ray data from September 2019 - March 2021. I did not design the cosmic ray testing procedure nor write the data preparation software, but I participated in using the software to analyze cosmic ray results. In the thesis, the terms “clustering,” “local offset” and “relative local offset” are defined. Cosmic ray clustering was done in the data preparation software, but I redid the fit afterwards to explore sensitivity to the fit algorithm. With help from Dr. Lefebvre and Dr. Vachon, I helped design the software that calculated the relative local offsets from cosmic ray data. I wrote that software on my own. I was not involved in the design, data collection, data preparation or analysis of the x-ray data. I also was not involved in creating an alignment model from the x-ray data. I used the x-ray local offsets calculated using x-ray data analysis software to calculate relative local offsets with x-rays. I did the comparison between the x-ray and cosmic ray data.

I hereby declare that I am the sole author of this thesis. This is a true copy of the thesis, including any required final revisions, as accepted by my examiners.

<sup>147</sup>

# Chapter 1

<sup>148</sup>

## Introduction

<sup>149</sup> The Standard Model (SM) is a theoretical framework that describes experimental observa-  
<sup>150</sup> tions of particles and their interactions at the smallest distance scales; however, the questions  
<sup>151</sup> the SM does not address motivate more experimentation.

<sup>152</sup> Accelerators collide particles to generate interactions that can be recorded by detectors  
<sup>153</sup> for further study. Detectors measure the trajectory and energy of all secondary particles  
<sup>154</sup> produced in collisions to understand the interaction. The Large Hadron Collider (LHC) [1]  
<sup>155</sup> at CERN is the world's most energetic particle accelerator. Its energy makes it a unique  
<sup>156</sup> tool to study elementary particles and their interactions in an environment with conditions  
<sup>157</sup> similar to what would have existed in the early universe. If study at the energy frontier is  
<sup>158</sup> to continue, the LHC must go on.

<sup>159</sup> After 2025, the statistical gain in running the LHC further without significant increase in  
<sup>160</sup> beam intensity will become marginal. The High Luminosity Large Hadron Collider (HL-  
<sup>161</sup> LHC) project [2] is a series of upgrades to LHC infrastructure that will allow the LHC  
<sup>162</sup> to collect approximately ten times more data than in the initial design by  $\sim$ 2030. The  
<sup>163</sup> increase in LHC beam intensity will result in a large increase in collision rate that will make  
<sup>164</sup> accessible and improve statistics on several measurements of interest [3], many only possible  
<sup>165</sup> at the LHC and the energy frontier. The increase in beam intensity will also increase the  
<sup>166</sup> level of background radiation, requiring major upgrades to the experiments used to record  
<sup>167</sup> the outcomes of the particle collisions.

<sup>168</sup> The ATLAS experiment [4] is one of the LHC's general-purpose particle detector arrays, po-  
<sup>169</sup> sitioned around one of the collision points of the LHC. During the 2019-2022 Long Shutdown  
<sup>170</sup> of the LHC, the most complex upgrade of the ATLAS experiment is the replacement of the  
<sup>171</sup> small wheels of the muon spectrometer with the so-called New Small Wheels (NSWs) [5].

172 The detector upgrade addresses both the expected decrease in hit efficiency of the precision  
173 tracking detectors and the high fake trigger rate expected in the muon spectrometer at the  
174 HL-LHC. The NSWs are made of two different detector technologies: micromegas and small-  
175 strip thin gap chambers (sTGCs). Micromegas are optimized for precision tracking while  
176 sTGCs are optimized for rapid triggering, although each will provide complete coverage and  
177 measurement redundancy over the area of the NSWs. Eight layers each of sTGCs cover the  
178 NSWs. Practically, countries involved in detector constructor created quadruplet modules of  
179 four sTGCs glued together that were arranged and installed over the area of the NSWs once  
180 they arrived at CERN. Teams across three Canadian institutions built and characterized 1/4  
181 of all the required sTGCs.

182 The sTGCs are gas ionization chambers that consist of a thin volume of gas held between two  
183 cathode boards. One board is segmented into strip readout electrodes of 3.2 mm pitch. The  
184 position of the particle track in the precision coordinate can be reconstructed from the strip  
185 signals [5]. The sTGCs achieved the design track spatial resolution in the precision coordinate  
186 of less than 100  $\mu\text{m}$  per detector plane that will allow them to achieve a 1 mrad track angular  
187 resolution using the 8 layers of sTGC on the NSW [6, 5]. The NSW measurement of the  
188 muon track angle will be provided to the ATLAS trigger and used to reject tracks that do  
189 not originate from the interaction point [5].

190 The precise measurement of a muon track angle depends on knowing the position of each  
191 readout strip within the ATLAS coordinate system. To achieve this, the position of specific  
192 locations on the surface of sTGC quadruplets will be monitored by the ATLAS alignment  
193 system to account for time-dependent deformations [5]. Within a quadruplet module, the  
194 strip positions could have been shifted off of nominal by non-conformities of the strip pattern  
195 etched onto each cathode boards [7] and shifts between strip layers while gluing sTGCs into  
196 quadruplets.

197 An xray gun was used to measure the offset of strips from their nominal position at the  
198 locations that will be monitored by the ATLAS alignment system thereby providing, locally,  
199 an absolute “as-built” strip position within the ATLAS coordinate system. Estimates of the  
200 “as-built” positions of every readout strip are obtained by building an alignment model from  
201 the available x-ray measurements [8].

202 The technique of measuring the “as-built” strip positions using xray data has never been  
203 used before and must be validated. This thesis describes the use of cosmic muon data,  
204 recorded to characterize the performance of each Canadian-made sTGC module, to validate  
205 the x-ray strip position measurements. A description of how this work fits within the overall  
206 alignment scheme of the NSW is also presented.

207 *Rewrite after implementing Brigitte’s edits.* Chapters 3 and 4 give more background on  
208 particle physics, the LHC, ATLAS, the NSWs, and sTGCs. In chapter 5, the cosmic ray

209 testing procedure and how the position of the strips can be probed with cosmics data is  
210 presented. Chapter 6 introduces the x-ray method, and in chapter 7, the x-ray offsets are  
211 validated with cosmic muon data. The thesis concludes with a summary and outlook in  
212 chapter 8.

# <sup>213</sup> Chapter 2

## <sup>214</sup> High energy particle physics

<sup>215</sup> Particle physics aims to study the elementary constituents of matter. Understanding the fundamental building blocks and how they interact provides insight into how the early universe evolved to the forms of matter we observe today. This chapter introduces general concepts in particle physics relevant to understanding the physics goals of the High-Luminosity LHC (HL-LHC) and NSWs upgrade.

<sup>220</sup> The information on particle physics and the SM presented here is rather general; the interested reader is referred to [9, 10, 11] for more information.

### <sup>222</sup> 2.1 The Standard Model

<sup>223</sup> The Standard Model (SM) is a theoretical framework developed in the early 1970's that describes the observed elementary particles and their interactions. It is built on a collection of quantum field theories and has been remarkably successful at predicting experimental observations, including but not limited to the existence of the top quark [12], the tau neutrino [13] and the Higgs boson [14, 15].

<sup>228</sup> The known elementary particles described by the SM are represented in figure 2.1. There are 12 matter particles (six quarks and six leptons), 4 force-mediating particles, and the Higgs boson. Each matter particle also has an anti-matter particle pair with the same mass but opposite charge, not represented in figure 2.1. The different forces of nature are understood to be the result of the exchange of force-mediating particles between interacting (coupled) particles. Photons are mediators of the electromagnetic force, W<sup>+</sup>/- and Z bosons are mediators of the weak force, and gluons are mediators of the strong force. At high

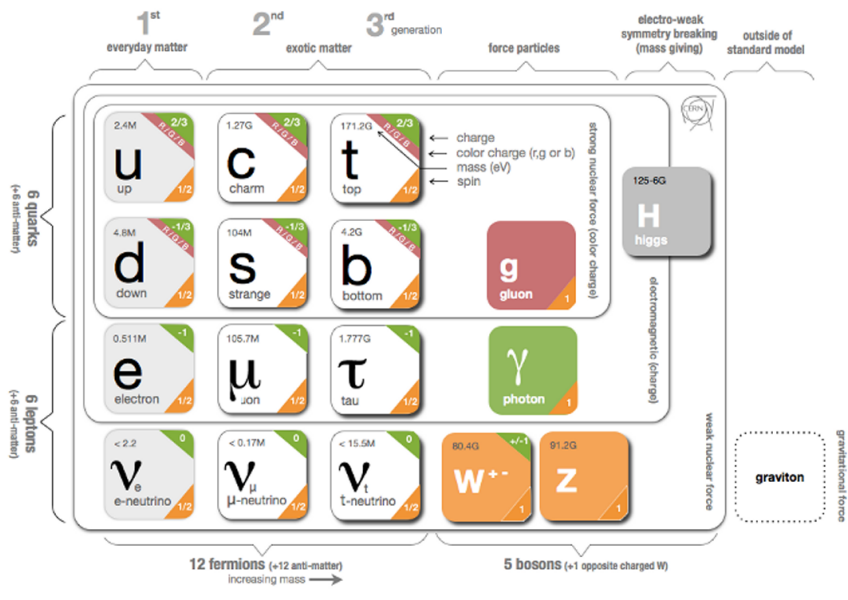


Figure 2.1: Schematic diagram of all elementary particles in the SM. Particles are grouped according to their properties and the forces through which they interact with other particles [16].

235 energy, the SM describes the electromagnetic and weak forces as stemming from a unified  
236 electroweak force. The Higgs boson field interacts with the particles mediating the unified  
237 electroweak force to distinguish the weak and electromagnetic forces from each other at lower  
238 energies and give particles (except neutrinos) a mass. This is called electroweak symmetry  
239 breaking.

240 Quarks are matter particles that are sensitive to all forces; notably they are the only particles  
241 sensitive to the strong force. Protons and neutrons are made up of quarks and gluons, and the  
242 strong force is responsible for their existence and mutual attraction into nuclei [17]. Leptons  
243 are particles not sensitive to the strong force. Charged leptons include the electron, which  
244 once part of atoms is responsible for chemistry. Of particular importance for this thesis is  
245 the charged lepton called a muon. It is like the electron but its mass is  $\sim$ 200 times larger  
246 than that of the electron. Muons have a lifetime of  $2.2\ \mu\text{s}$  [11] and decay predominantly as  
247  $\mu \rightarrow e^-\bar{\nu}_e\nu_\mu$ . Neutrinos are neutral, almost massless leptons that only interact through the  
248 weak force.

249 Common matter is made up of the lightest constituents of the SM: up and down quarks,  
250 electrons and photons. The other particles are produced in high-energy environments but  
251 then decay to the lightest constituents. Such high energy environments include the condi-  
252 tions present in the early universe [18], astrophysical sources, and particle accelerators. The  
253 presence of the particles of the SM at the beginning of the Universe means that their inter-  
254 actions and decays are fundamental for the study of the evolution of the early universe [18].  
255 Many high energy astrophysical sources, like supernovae, generate particles that rain down  
256 on Earth as cosmic rays [19]. Particle accelerators have been built to create controlled en-  
257 vironments of high-rate, high-energy particle collisions at high energy where the production  
258 and decay of elementary particles can be directly studied.

## 259 2.2 Beyond the Standard Model

260 Despite its success at describing most experimental observations to date, there is ample  
261 evidence that the SM is not a complete description of natural phenomena at the smallest  
262 scales. For example, the SM has a large number of free parameters, the values of which have  
263 to be fine-tuned to fit experimental observations. This is part of the so-called “naturalness”  
264 problem.

265 Furthermore, the SM provides no explanation for several open questions in particle physics.  
266 First, neutrinos in the SM are assumed to be massless and do not gain mass in the same way  
267 as the other particles. However, neutrino were confirmed to change between their different  
268 flavours in 2013 [20], which can only occur if neutrinos do have mass [21]. The neutrino

269 mass requires physics beyond the standard model [22]. Second, several astrophysical and  
270 cosmological measurements suggest the presence of “dark matter” making up 85 % of the  
271 matter content of the universe [23]. The nature of dark matter is unknown and so far there  
272 is no SM explanation [24]. Third, the SM does not explain the origin and nature of the  
273 matter-antimatter asymmetry that produced our matter-dominated universe. Finally, the  
274 SM does not include a description of gravity.

275 Theoretical extensions beyond the Standard Model (BSM) aim to address some of these  
276 questions, often predicting existence of yet-unseen elementary particles or physics phenomena  
277 beyond those predicted by the SM. For example, super-symmetry (SUSY) predicts that each  
278 SM particle has a heavier super-symmetric partner. SUSY would explain the origin of dark  
279 matter with weakly interacting massive particles, would solve the so-called “naturalness”  
280 problem in the SM [25]. These hypothetical new physics phenomena or new particles can be  
281 searched for at particle accelerators.

## 282 **2.3 Studying high energy particle physics with accelerators**

284 In particular, particle accelerators of increasingly higher energy have a long history of enabling  
285 the discovery of predicted particles. These include, for example, the discovery of  
286 the W [26, 27] and Z bosons [28, 29], the top quark [30, 31], and most recently, the Higgs  
287 boson [32, 33]. The discovery of the Higgs boson marked the completion of the SM as it is  
288 known today.

289 Based on the established success of the SM, there are two approaches to particle physics  
290 research. One approach is to search for the existence of new physics phenomena predicted  
291 to exist in BSM theories and the other is to test the validity of the SM to a high degree of  
292 accuracy to search for flaws in the model. Standard Model predictions are generally expressed  
293 in terms of the probability of a specific physics process to occur, expressed as a cross section  
294 in units of barns (with 1 barn =  $10^{-28}$  m<sup>2</sup>). As an example, figure 2.1 shows a summary  
295 of cross section measured for different physics processes using the ATLAS experiment and  
296 their comparison with the predictions of the SM. Most cross section measurements agree  
297 well within one standard deviation with the SM predictions.

298 Particle accelerators provide a controlled and high-collision rate environment that makes  
299 them ideal places to search for new physics phenomena and to carry out systematic tests of  
300 the SM. The LHC is the highest energy collider in the world so it can access physics that  
301 no other accelerator can. A description of the LHC and the ATLAS detector are provided  
302 in the next chapter.

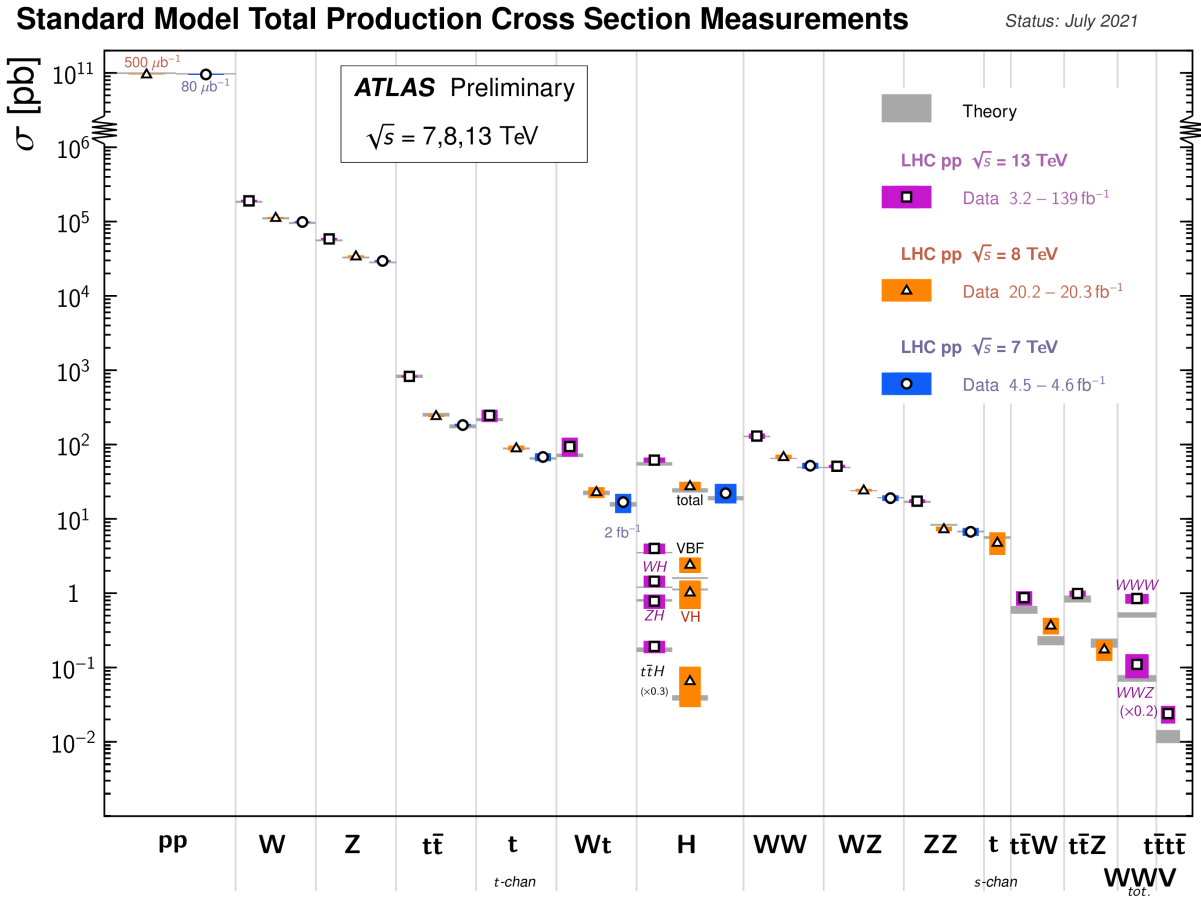


Figure 2.2: Production cross sections of different final states measured by the ATLAS experiment at the LHC. Comparison with the SM theory predictions is also shown [34].

303 **Chapter 3**

304 **The LHC and the ATLAS experiment**

305 The Large Hadron Collider (LHC) is the world's most energetic particle accelerator and the  
306 ATLAS experiment is used to record the results of particle collisions at the LHC. In this  
307 chapter, details about both that are necessary to understand the High-Luminosity LHC (HL-  
308 LHC) upgrade project and the ATLAS experiment's New Small Wheels (NSWs) upgrade  
309 are presented.

310 **3.1 The Large Hadron Collider**

311 The LHC is an accelerator 27 km in circumference and located  $\sim$ 100 m underground at  
312 the CERN laboratory near Geneva, Switzerland [1]. It has two beam pipes within which  
313 bunches of protons counter-circulate before being collided in the center of one of four major  
314 experiments, such as the ATLAS experiment (discussed in section 3.3). Protons are guided on  
315 the circular trajectory using 1232 superconducting dipole magnets capable of a maximum  
316 field of 8.33 T. Radio-frequency accelerating cavities are used to accelerate protons to a  
317 the maximum design energy of 7 TeV [35]. During LHC Run-1 (2011-2012), protons were  
318 collided at a collision center-of-mass energy of 7 TeV and 8 TeV [36]. During LHC Run-2  
319 (2015-2018), the center-of-mass energy of proton collisions was increased to 13 TeV [37],  
320 close to the maximum design value of 14 TeV [35]. It is not actually the protons that  
321 interact, but the constituent quarks and gluons that each carry some fraction of the energy  
322 and momentum of the collisions.

323 **Luminosity**

324 The number of proton-proton interactions generated by the LHC directly affects the statistics

available to make measurements of interaction cross sections. Predicting the number of proton-proton interactions requires defining a metric called luminosity [11]. The luminosity of a particle collider is the number of particles an accelerator can send through a given area per unit time. It is calculated from the measurable quantities in Equation 3.1:

$$\mathcal{L} = \frac{f N_1 N_2}{4\pi\sigma_x\sigma_y}, \quad (3.1)$$

where  $f$  is the frequency of the bunch crossings (25 ns),  $N_1$  and  $N_2$  are the number of protons in each bunch ( $\sim 10^{11}$  protons / bunch), and  $\sigma_x$  and  $\sigma_y$  are the RMS of the spatial distributions of the bunch. Therefore, luminosity is a property of accelerator beams, which are set by the capabilities of the accelerator. The design luminosity of the LHC was  $10^{34} \text{ cm}^{-2}\text{s}^{-1}$ . The units of luminosity are an inverse area; multiplying the luminosity by the cross section of a given process gives the expected rate for that process.

Integrating the *instantaneous* luminosity (equation 3.1) over a period of data collection time gives the integrated luminosity,

$$L = \int \mathcal{L}(t) dt \quad (3.2)$$

which is related to the total number of interactions. In this way, the luminosity is the link between the accelerator and the statistical power of measurements to be made with the data collected. So far, the LHC provided an integrated luminosity of  $28.26 \text{ fb}^{-1}$  in Run-1 [36] and  $156 \text{ fb}^{-1}$  in Run-2 [37].

## 3.2 The High-Luminosity LHC

At the end of the LHC program in 2025, the statistical gain on measurements in running the LHC further will become marginal. The HL-LHC [2] project consists of the upgrade of LHC infrastructure to achieve a nearly ten fold increase in instantaneous luminosity, thereby improving measurement statistics as well. Also, some systems will need repair and replacement to operate past  $\sim 2020$ . The LHC will continue to be the most energetic accelerator in the world for years to come and is the only accelerator with enough energy to directly produce the Higgs boson and top quarks. Therefore, the European Strategy for Particle Physics made it a priority “to fully exploit the physics potential of the LHC” with “a major luminosity upgrade” [38]. The goal is for the HL-LHC to provide an integrated luminosity of  $3000 \text{ fb}^{-1}$  in the 12 years following the upgrade. The luminosity actually



Figure 3.1: The LHC/HL-LHC timeline [39]. The integrated luminosities collected and projected for each run of the LHC are shown in blue boxes below the timeline and the center of mass energy of the collisions is shown in red above the timeline. The top blue arrow labels the run number. The acronym “LS” stands for “long shutdown” and indicates periods where the accelerator is not operating. During the shutdowns, upgrades to the LHC and the experiments are taking place. This timeline was last updated in January, 2021, and reflects changes in the schedule due to the ongoing pandemic.

352 achieved will depend on a combination of technological advances and upgrades in progress  
 353 that affect the factors contributing to luminosity defined in equation 3.1 [2]. Figure 3.1 shows  
 354 the projected schedule of the HL-LHC upgrades and operation [39].

355 One of the most anticipated measurements at the HL-LHC is the value of the triple-Higgs  
 356 coupling. Measuring the coupling will allow the determination of the shape of the Higgs  
 357 potential responsible for electroweak symmetry breaking. Any discrepancy with respect to  
 358 the SM prediction will show that there must be other sources of electroweak symmetry  
 359 breaking, and hence physics phenomena beyond the SM. The LHC is the only accelerator  
 360 where the Higgs boson can be produced directly so it is the only place where the triple-Higgs  
 361 coupling could be measured. The HL-LHC upgrade is required to produce a significant  
 362 sample of Higgs produced in pairs to make a statistically meaningful measurement [3, 40].

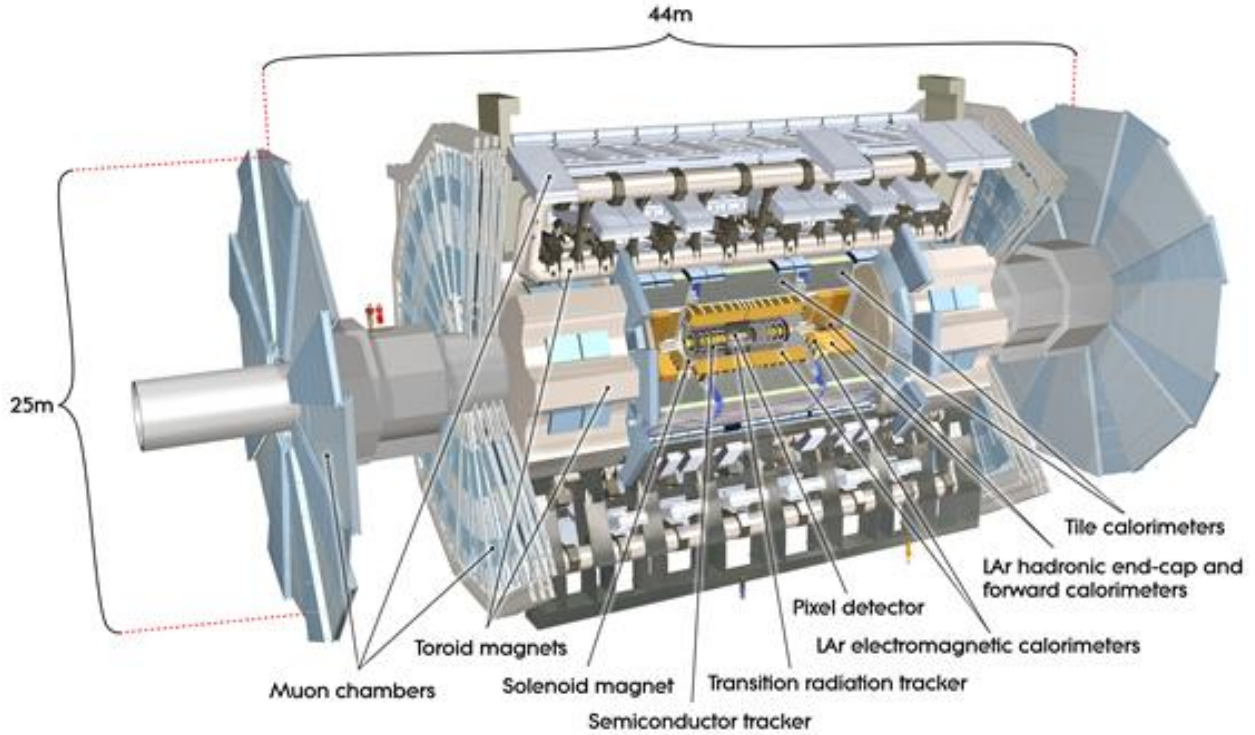


Figure 3.2: Schematic diagram of the ATLAS experiment, with the various detector subsystems labelled [4].

363 Accordingly, detector sensitivity to various Higgs decays will be important at the HL-LHC.

### 364 3.3 The ATLAS experiment

365 The ATLAS experiment [4] was designed to support all the physics goals of the LHC. It  
366 is 44 m long and 25 m in diameter, and weighs 7000 tonnes. The ATLAS experiment is  
367 centered around one of the LHC's interaction points (a place where the beams collide). As  
368 shown schematically in figure 3.2, ATLAS consists of an array of particle detector subsystems  
369 arranged concentrically around the beam pipe. The ATLAS experiment is cylindrical because  
370 it aims to provide  $4\pi$  coverage around the interaction point. In reference to the cylindrical  
371 geometry of the experiment, it is helpful to separate the subsystems of ATLAS into the  
372 so-called "barrel" and "endcap"/"forward" regions.

373 For analysis purposes, a spherical coordinate system is defined. The azimuthal angle  $\phi$  is  
374 measured around the beampipe and the polar angle  $\theta$  is measured from the beam pipe. The  
375 polar angle is more often expressed in terms of pseudo-rapidity, defined as  $\eta = -\ln \tan(\theta/2)$ .  
376 Pseudo-rapidity values vary from 0 (perpendicular to the beam) to  $\pm\infty$  (parallel to the  
377 beam, defined as the z-direction) and is an approximation to the rapidity of a particle when  
378 its momentum is much greater than its mass. It is useful to describe the direction of outgoing  
379 particles in proton-proton collisions because differences in rapidity are invariant to a Lorentz  
380 boost along the beam direction.  
381 The ATLAS experiment provides identification and kinematic measurements for each particle  
382 created after the initial collision, which is done by assembling offline the information recorded  
383 by each subsystem. With this information, signatures of processes of interest can be identified  
384 and studied. An overview of the main ATLAS subsystems is given below.

385 **The inner detector**  
386 The inner detector [41, 42] (figure 3.3) is for precise measurements of charged particle tra-  
387 jectories, measurement of primary and secondary interaction vertices and assistance in the  
388 identification of electrons. A 2 T solenoid with field parallel to the beam bends the trajec-  
389 tory of outgoing charged particles. A measurement of the bending radius of each charged  
390 particle provides information about its momentum. The innermost part of the inner tracker  
391 is made of high-resolution semiconductor pixel and strip detectors while the outermost part  
392 is made of straw-tubes. The straw tubes are used in the trajectory measurements but they  
393 are also interspersed with material designed to enhance the creation of transition radiation.  
394 Transition radiation occurs when a highly relativistic charged particle traverses a material  
395 boundary [43]. The amount of transition radiation emitted by a charged particle is detected  
396 by the straw-tubes and is used to identify electrons.

397 **Calorimetry system**  
398 Electromagnetic and hadronic sampling calorimeter units are used to record the energy  
399 of electrons, photons and jets<sup>1</sup>. A combination of liquid-argon (LAr) electromagnetic and  
400 hadronic calorimeters [44] and tile-scintillator hadronic calorimeters [45] cover the rapidity  
401 range  $|\eta| < 4.9$ , as shown in figure 3.4.  
402 Sampling calorimeters have alternating layers of dense material and material that can mea-  
403 sure the amount of ionization by charged particles. The dense material causes incoming

---

<sup>1</sup>When quarks or gluons are expelled in a high energy collision, they create collimated groups of hadrons because they carry a charge called “colour”, and nature only allows “colourless” combinations to exist [43].

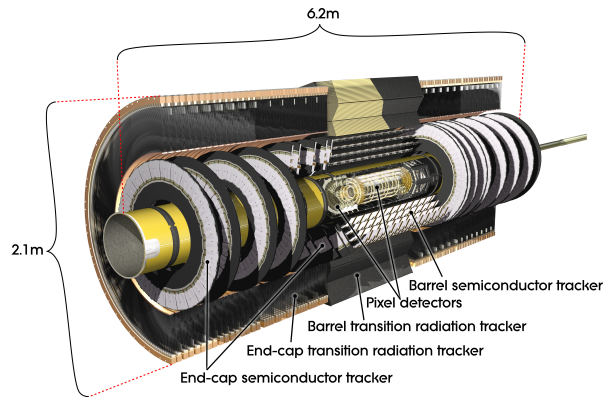


Figure 3.3: Schematic diagram of the ATLAS experiment's inner detector, with the different segments and the technology used labeled [4].

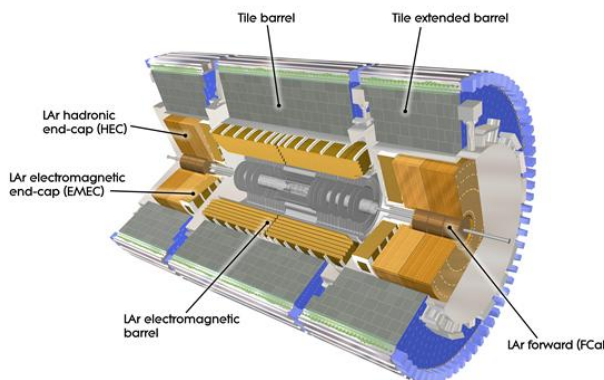


Figure 3.4: Schematic diagram of the ATLAS calorimeter system, with the different segments and the technology used labeled [4].

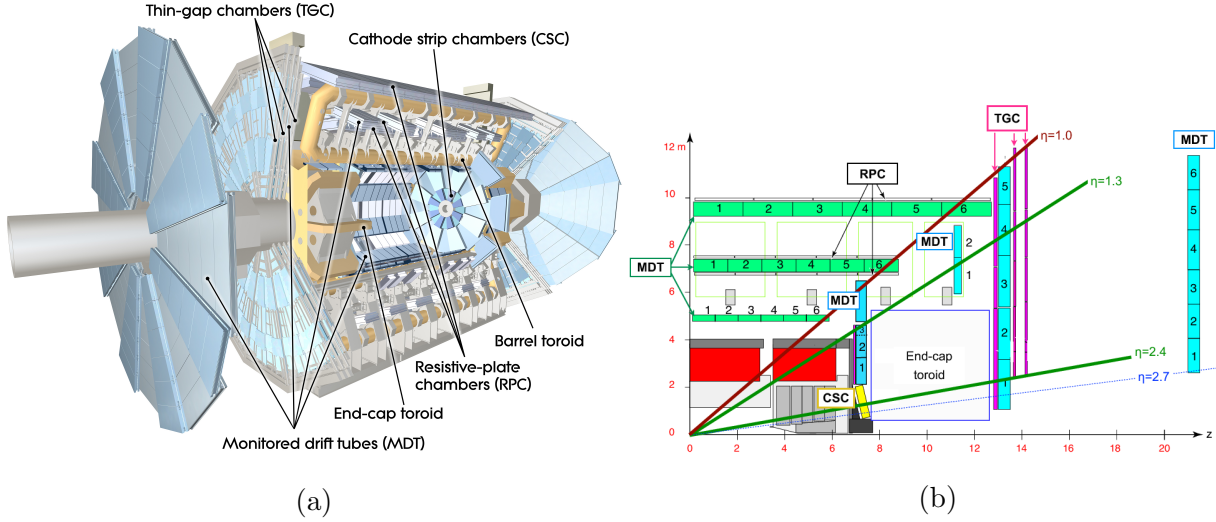


Figure 3.5: Schematic diagram of the ATLAS muon spectrometer. Figure (a) shows a 3D projection of the system with the different types of chambers and different parts of the toroidal magnet system labeled [4]. Figure (b) shows a projection of one quarter of the muon spectrometer, with the interaction point in the bottom left corner. The small wheel is just left of the end cap toroid, the big wheel is to its right, and the outer wheel is the rightmost structure [48].

404 charged particles to shower into lower energy particles and deposit their energy in the sen-  
 405 sitive volume. Only muons and neutrinos are known to pass the calorimeters to the muon  
 406 spectrometer without being absorbed.

#### 407 Muon spectrometer

408 The muon spectrometer [46] consists of multiple layers of tracking chambers embedded in  
 409 a 2 T magnetic field generated by an air-core superconducting toroid magnet system. Fig-  
 410 ure 3.5a shows a schematic diagram of the layout of the different chambers and of the toroid  
 411 magnets [4]. The trajectory of a muon is reconstructed from the information recorded by  
 412 the different types and layers of tracking chambers. The amount of bending in the magnetic  
 413 field provides a measure of the muon's momentum. In the barrel section of ATLAS, the  
 414 toroidal magnetic field is created by eight coils bent into the shape of a "race-track" and  
 415 symmetrically arranged around the beampipe. In the forward region, two end-cap toroids,  
 416 each with eight smaller racetrack-shaped coils arranged symmetrically around the beam pipe  
 417 are inserted in the ends of the barrel toroid [47].

418 The muon spectrometer is separated into detectors used for precision offline tracking and

419 for triggering purposes. Three layers of monitored drift tubes (MDTs) or cathode strip  
420 chambers (CSCs) are used for tracking. The position of the muon track in each of the three  
421 layers allows reconstruction of the bent trajectory of a muon and hence its momentum. To  
422 satisfy the muon spectrometer target momentum resolution of  $\Delta p_T/p_T < 1 \times 10^{-4}$   $p$  / GeV  
423 for  $p_T < 300$  GeV and a few percent for lower  $p_T$  muons, the MDTs and CSCs were designed  
424 to achieve a spatial resolution of 50  $\mu\text{m}$  each. Accordingly, an optical alignment system was  
425 designed to monitor and correct for chamber positions [46, 49].

426 Resistive plate chambers (RPCs) are used for triggering in the barrel and thin-gap chambers  
427 (TGCs) are used for triggering in the endcaps. The positions of each type of chamber  
428 are sketched in figure 3.5b. The endcap section of the muon spectrometer consists of three  
429 sections, the small wheel, big wheel, and outer wheel – ordered by proximity to the interaction  
430 point. In Run-1, low (high)  $p_T$  muons were triggered on if two (three) of the RPC or TGC  
431 layers around the big wheel fired in coincidence, for the barrel and endcaps respectively [50].  
432 After Run-1 it was discovered that up to 90% of the triggers in the endcap were fake, caused  
433 by background particles generated in the material between the small wheel and the big  
434 wheel [5]. To reduce the fake rate in Run-2, the TGCs on the inside of the small wheel also  
435 had to register a hit. The added condition reduced the trigger rate by 50% in the range  $1.3 < |\eta| < 1.9$  [51]. The effectiveness of the solution was limited since the  $|\eta|$ -range of the small  
437 wheel TGCs was limited to  $1.0 < |\eta| < 1.9$  and the spatial resolution of the small wheel  
438 TGCs is coarse [5].

### 439 Trigger system

440 It would be impossible to record all the data from bunch crossings every 25 ns, corresponding  
441 to a rate of  $\sim 40$  MHz. The ATLAS experiment has a multi-level trigger system to select  
442 events of interest for permanent storage. The Level-1 (L1) hardware trigger [50] uses partial-  
443 granularity information from the muon spectrometer and calorimeters to trigger on high  $p_T$   
444 muons, electrons, jets, missing transverse energy, and  $\tau$  decaying to hadrons. After Run-3  
445 an upgrade of the trigger system will allow a maximum trigger rate of 1 MHz with a latency  
446 of 10  $\mu\text{s}$  [52], but for now the working limits are a rate of 100 kHz [51] and 2.5  $\mu\text{s}$  [50].

447 The L1 trigger is used to define regions of interest that are fed into the software high level  
448 trigger (HLT) [53], in which the full granularity of the muon spectrometer and calorimeter  
449 are used with information from the inner detector to reduce the trigger rate to 1 kHz. Events  
450 that satisfy at least one of the L1 and HLT trigger criteria are recorded to permanent storage  
451 for offline analysis.

453 With the foreseen increase in luminosity at HL-LHC, it is a priority to upgrade the ATLAS  
454 detector to further reduce the muon trigger fake rate in the forward region. The New Small  
455 Wheels being commissioned to replace the original ATLAS muon small wheels will address  
456 this challenge.

457 **Chapter 4**

458 **The New Small Wheels**

459 **4.1 Motivation for the New Small Wheels (NSWs)**

460 The hit rate of all detector systems will increase with the HL-LHC not only because of the in-  
461 crease in luminosity, but also because the background radiation rate increases proportionally  
462 with luminosity. The combined rate presents problems for both the tracking and triggering  
463 capabilities of the muon spectrometer [5].

464 In term of tracking, the efficiency of the MDTs decreases by 35% (mostly due to long dead-  
465 times) already when exposed to the maximum hit rate at the current luminosity, 300 kHz.  
466 At the threefold increase in luminosity predicted for Run-3, most of the small wheel will be  
467 subjected to a hit rate well above 300 kHz and it will begin missing hits. Losing hits in the  
468 small wheel will reduce the high  $p_T$  muon momentum resolution. The decrease in resolution  
469 will affect the ability to search for, for example, the decay of heavy bosons ( $W'$ ,  $Z'$ ) or a  
470 pseudo-scalar Higgs predicted by some SUSY models [3].

471 Already, the forward muon trigger system copes with a very high fake rate, even when  
472 including TGC data from the small wheel in the trigger as in Run-2. At the luminosity  
473 expected in Run-3, 60 kHz of the maximum 100 kHz of the L1 trigger would be taken by the  
474 endcap muon spectrometer. A possible solution would be to raise the minimum  $p_T$  threshold  
475 from 20 GeV to 40 GeV, but the ability to study several physics processes of interest depend  
476 on low  $p_T$  muons, particularly the Higgs decay to two muons, the Higgs decay to two tau's  
477 and SUSY particle decays to leptons [5].

478 The NSWs will solve both these problems. It will be covered with precision tracking cham-  
479 bers suitable for the expected hit rates and triggering chambers capable of 1 mrad angular

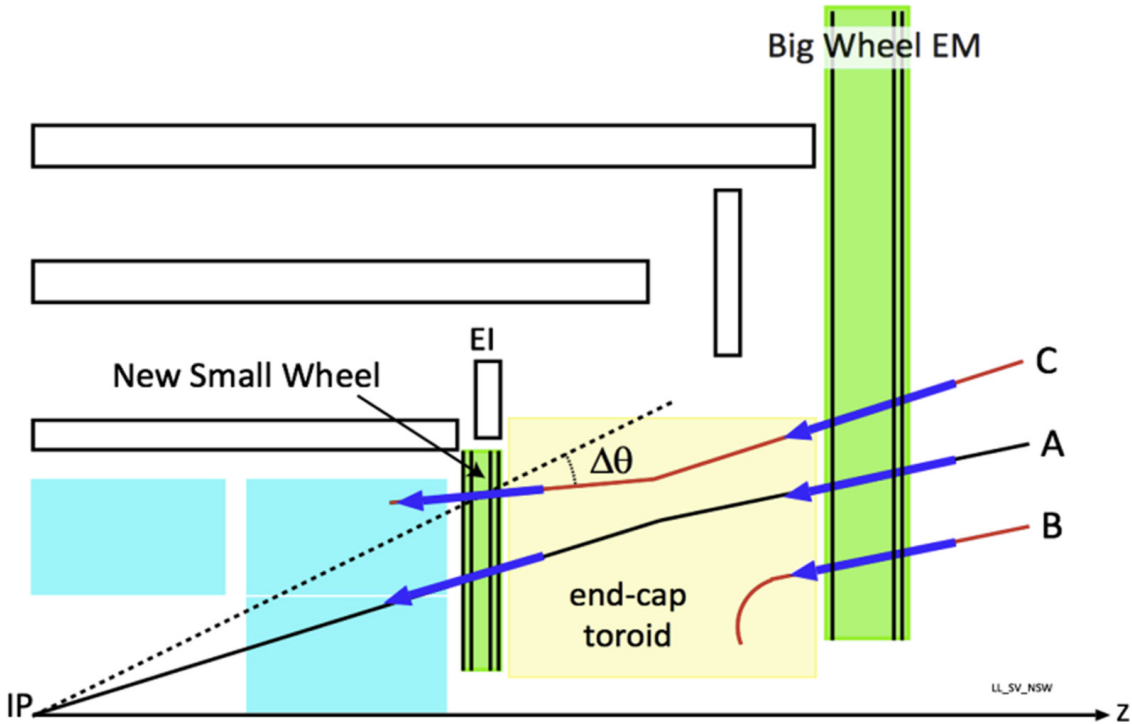


Figure 4.1: A schematic of a quarter cross section of the ATLAS detector, with the collision/interaction point (IP) in the bottom left corner. Three possible tracks are labelled. Ideally, track A would be triggered on while track B and C discarded. With the small wheel, all three tracks would be recorded. With the NSW, only track A would be recorded [5].

480 resolution. The idea behind the triggering chambers is to match the small wheel track seg-  
 481 ment with the track segment from the big wheel to discard tracks not originating from the  
 482 interaction point. Figure 4.1 illustrates this point: the Run-1 trigger system would have  
 483 triggered on all three tracks, while with the NSW the trigger system would only trigger on  
 484 track A. Reducing the fake trigger rate means the NSWs will not miss as many muon hits  
 485 and that the low  $p_T$  threshold will not have to be raised to cut particles not produced in the  
 486 collision. The NSWs allow ATLAS to maintain the high  $p_T$  muon resolution and the low  
 487 muon  $p_T$  threshold at the HL-LHC collision rate [5].

488 **4.2 Design of the NSWs**

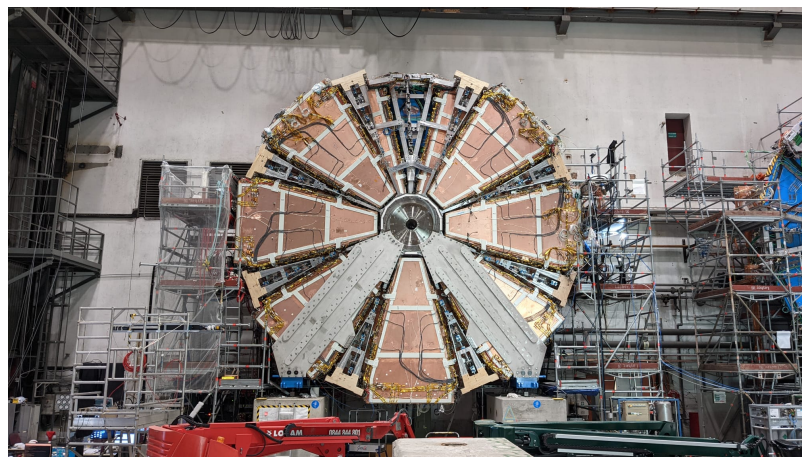
489 The NSWs are covered with two detector technologies: micromegas and small-strip thin gap  
490 chambers. MMs are the primary tracking detectors and sTGCs are the primary triggering  
491 detectors, but for redundancy sake both are designed to do either. Both sets of detectors are  
492 to have position resolution better than  $\sim 100 \mu\text{m}$  per plane. Four chambers of each type are  
493 glued together to create quadruplet modules. Quadruplets of different sizes are assembled  
494 into wedges. Two sTGC wedges and two MM wedges are layered to create sectors (with  
495 the sTGC wedges on the outside) [5]. Different stages of the construction process are shown  
496 in figure 4.2. At the time of writing, both NSWs have been assembled. The first has been  
497 lowered into the ATLAS cavern and is being commissioned. The second will be lowered  
498 shortly.



(a) An sTGC quadruplet module. The left image highlights the trapezoidal shape. The right image shows the short edge corner. The four sTGC layers and each layer's gas inlet are visible. The gas outlets and high voltage cables are at the long edge in the back of the photo. The green printed circuit board along the sides are the adaptor boards where the front end electronics are attached.



(b) Left: An sTGC wedge. The white frame outlines the individual quadruplet modules. Right: A completed sector, with two sTGC wedges on the outside and two MM wedges on the inside.



(c) The New Small Wheel. All sectors except one large sector at the top are installed, revealing two of the smaller sectors that are normally hidden under the large sectors and support bars. The NSWs are 10 m in diameter.

Figure 4.2: Images breaking down some of the construction units of the NSWs.

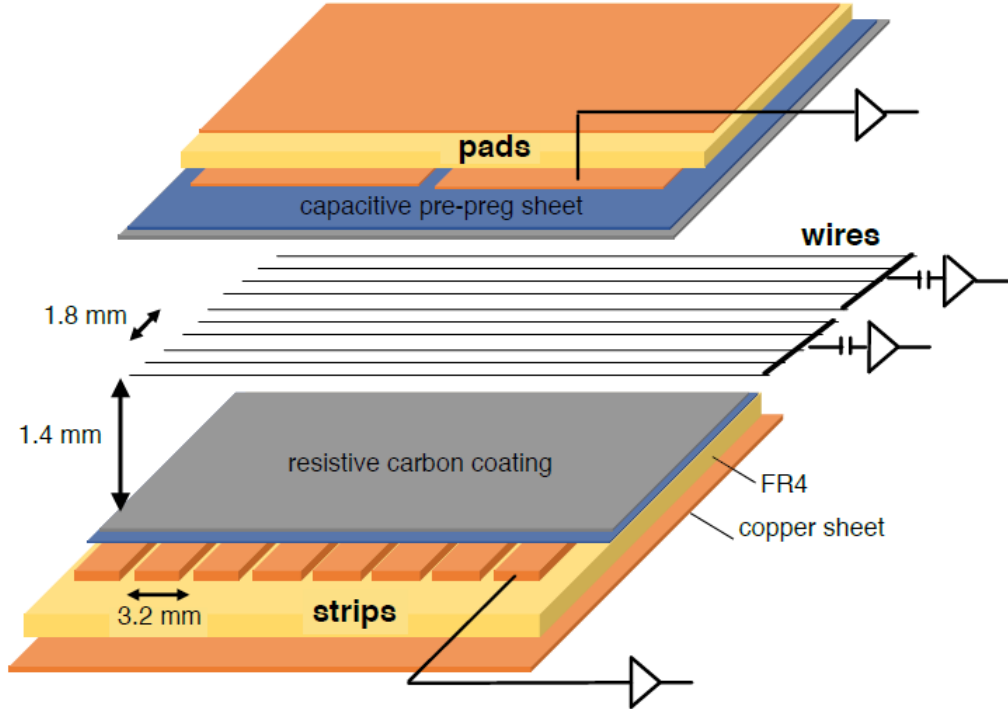


Figure 4.3: Internal structure of an sTGC, zoomed into the area under a pad. High voltage is applied to wires suspended in the gas volume to create an electric field. A passing muon causes an ionization avalanche that is picked up by the wire, strip and pad electrodes [8].

### 499 4.3 Small-strip thin gap chambers

500 sTGCs are gas ionization chambers operated with a CO<sub>2</sub>:n-pentane ratio of 55:45. Gold-  
501 plated tungsten wires, 50 µm in diameter and with 1.8 mm pitch, are suspended between  
502 two cathode planes made of FR-4, each 1.4 mm away (see figure 4.3). One cathode board is  
503 segmented into pads of varying area (around 300 cm<sup>2</sup> each), and the other segmented into  
504 strips of 3.2 mm pitch, perpendicular to the wires. High voltage is applied to the wires and  
505 the cathode planes are grounded [5, 54]. When a muon passes through, the gas is ionized  
506 and the electric field in the gas gap causes an ionization avalanche [55]. The motion of the  
507 ions and electrons are picked up on the nearby wire, strip and pad electrodes [5]. The gas  
508 mixture was chosen to absorb excess photons produced in the avalanche that delocalize the  
509 avalanche signal [56]. The resistivity of the carbon coating and capacitance of the pre-preg

sheet tune the spread of the charge distribution [57] and the speed of the response [58] to optimize the rate capability. The hatching of the strips and wires establishes a coordinate system from which to extract the coordinate of the muon as it passes through the chamber. The small pitch of the strips is what allows the quadruplets to deliver good angular resolution to improve the fake trigger rate and meet the precision tracking requirements [5].

A 3-out-of-4 coincidence in pad electrodes from each layer of a quadruplet define a region of interest where the strip and wire electrodes should be readout. The pad triggering scheme greatly reduces the number of electrodes that require read-out so that a track segment of the required angular resolution can be provided quickly enough to the hardware trigger [5].

Signal is readout from groups of successive wires, so the position resolution in the direction perpendicular to the wires is 10 mm. The wires give the symmetric azimuthal coordinate in ATLAS so the position resolution in this direction is sufficient. Good resolution on the  $\eta$  coordinate, perpendicular to the strips, is important [5]. The average single chamber position resolution in the strip coordinate was 45  $\mu\text{m}$  for perpendicular muon tracks as measured in a test beam [6] – well within design specifications. When four sTGCs are glued together into a quadruplet the design angular resolution of 1 mrad in the strip coordinate is achievable [5, 54].

Therefore, sTGCs are able to meet the triggering and precision tracking goals they were designed for. To ensure they can deliver once installed in ATLAS, knowing the position of the strips to within their position resolution in the ATLAS coordinate system is necessary. The NSW alignment system, detailed in section 4.5, monitors the position of alignment platforms installed on the surface of the wedges. The alignment platforms are installed with respect to an external reference on the sTGCs: two brass inserts on each strip layer on one of the angled sides of each quadruplet (shown in figure 4.4). So the challenge of positioning the strips in ATLAS was separated into two steps: first, position the strips with respect to the brass inserts; second use the alignment system to position the alignment platforms. The next section provides some pertinent details on the sTGC construction process, with steps that affect the position of the strips with respect to the brass inserts highlighted.

## 4.4 sTGC Quadruplet Construction

Five countries were responsible for producing the sTGC modules of varying geometries for the NSW: Canada, Chile, China, Israel and Russia. Canada was responsible for 1/4 of the required sTGCs, of three different quadruplet geometries. The steps of the construction process in each country were similar [5]. The process followed in Canada is detailed.

TRIUMF in Vancouver, British Columbia was responsible for preparing the cathode boards. The boards were made and the electrodes etched on at a commercial laboratory, Triangle



(a) Brass insert near long edge.

(b) Brass insert near short edge.

Figure 4.4: The brass inserts sticking out from the gas volumes of an sTGC quadruplet. These inserts were pressed against alignment pins when the individual sTGCs were being glued together.

544 Labs, in Carson City, Nevada. Once completed they were sent to TRIUMF to be sprayed with  
545 graphite and otherwise prepared [7]. The boards are commercial multilayer printed circuit  
546 boards, but the strip boards required precision machining to etch the strip pattern [5].  
547 Triangle Labs also machined the two brass inserts into each strip board. A coordinate  
548 measuring machine (CMM) was used to digitize a set of reference strips. Four quality  
549 parameters describing non-conformities in the strip pattern of each board with respect to  
550 the brass inserts were derived from the data and the results are available on a QA/QC  
551 database. The parameters and the CMM data collection is described in full in [7]. Due to  
552 time constraints, tolerances on the non-conformities in the etched strip pattern with respect  
553 to the brass inserts were loosened, with the condition that the strip positions in ATLAS  
554 would have to be corrected for [7].

555 The prepared boards were sent to Carleton University in Ottawa, Ontario for construction  
556 into sTGCs and quadruplets. First, the wires were wound around the pad cathode boards  
557 using a rotating table and the wires were soldered into place. A wound pad cathode board  
558 was held by vacuum on a granite table, flat to within 20  $\mu\text{m}$ , and a strip cathode board glued  
559 on top to create an sTGC. Holding one sTGC flat with the vacuum, another was glued on  
560 top to create a doublet, then two doublets were glued together to create a quadruplet. When  
561 gluing sTGCs together, the brass inserts were pushed against alignment pins with the goal of  
562 keeping the strip layers aligned within tolerance. However, non-conformities in the shape of  
563 the brass inserts, non-conformities in the position of the alignment pins and shifts between  
564 sTGCs while the glue cured resulted in misalignments between the brass inserts and strip  
565 layers. Precise alignment of the pad boards or wires with respect to the strip boards did not  
566 have to be so tightly controlled because pads do not measure the precision coordinate.

567 The Carleton team finished the quadruplets by installing adaptor boards on the angled sides  
568 of each layer that allow front end electronics to be attached. Completed quadruplets were  
569 sent to McGill University where they were characterized with cosmic rays. The details of  
570 cosmic ray testing are described in chapter 5. Tested quadruplets were sent to CERN where  
571 they were assembled into wedges and alignment platforms installed. The alignment platforms  
572 were installed using a jig positioned with respect to the brass inserts. Completed wedges  
573 were assembled into sectors then installed on the NSWs.

574 The quadruplet construction process had two steps where strip positions could be shifted off  
575 of nominal. At board-level, there could be non-conformities in the etched strip pattern with  
576 respect to the brass inserts, described by the four quality parameters [7]. At the quadruplet  
577 level, misalignments between the brass inserts and strips on different layers were introduced  
578 during the gluing. The result was that the brass inserts were not a reliable reference point  
579 and that the strips can be offset from their design position by up to hundreds of micrometers.  
580 Offsets in strip positions from nominal in Canadian quadruplets were shown to be random [7],

581 so no one correction would suffice. The offsets must be measured and corrected for in the  
582 ATLAS offline software that does the precision tracking. Understanding the work ongoing  
583 to make measurements of offsets and correct for them requires understanding the strategy  
584 of the NSW alignment system.

## 585 4.5 NSW alignment

586 The idea of the NSW alignment system is presented in [5], but the details have only been  
587 presented internally so far. After the wedges are constructed, alignment platforms are in-  
588 stalled on every sTGC quadruplet and optical fibres routed to them, as shown in figure 4.5.  
589 Light from the optical fibres will be monitored in real time by cameras (BCAMs) mounted on  
590 the alignment bars of the NSWs. The system will thus record the positions of the alignment  
591 platforms in the ATLAS coordinate system, accessible at any point during operation.

592 The original alignment scheme was to use the brass inserts as a reference between the align-  
593 ment platforms and the individual strips, as shown in the solid arrows in figure 4.6 – this  
594 will no longer work. The position of the alignment platforms will be known thanks to the  
595 alignment system, so a different method to get the position of the strips with respect to  
596 the alignment platforms is currently in its final stages. It uses the yet-unmentioned x-ray  
597 dataset to calculate offsets of the strip pattern of an sTGC layer in a local area (local offset)  
598 with respect to the nominal geometry by analyzing the beam profile left by an x-ray gun  
599 attached to different positions on the alignment platforms. Effectively, the reference to the  
600 brass inserts is skipped, represented as the dashed line in figure 4.6. The alignment plat-  
601 forms provide the link to the nominal geometry because their position with respect to the  
602 strips can be calculated from the nominal geometric parameters assuming that the strips  
603 are perfectly etched and aligned. Cosmic muon track positions cannot be compared to the  
604 nominal geometry because the alignment platforms are not installed when cosmics data is  
605 collected, so there is no external reference to provide a link to the nominal geometry.

606 The x-ray method does not have the sensitivity to measure the offset of each strip from  
607 nominal, but instead the offset of the strip pattern in a local area around the position of  
608 the gun can be measured. *Local offsets* are used to build an alignment model for each strip  
609 layer. Formally defined, an alignment model is a set of parameters used to estimate the true  
610 position of a strip given its nominal position. The alignment model currently being worked  
611 on takes x-ray and CMM data as input to calculate an offset and rotation of each strip  
612 layer with respect to nominal [8]. The alignment parameters could be described as “global”,  
613 meaning over the whole layer instead of local. Without the x-ray dataset, there would be no  
614 input to the alignment model that takes into account inter-layer misalignments introduced

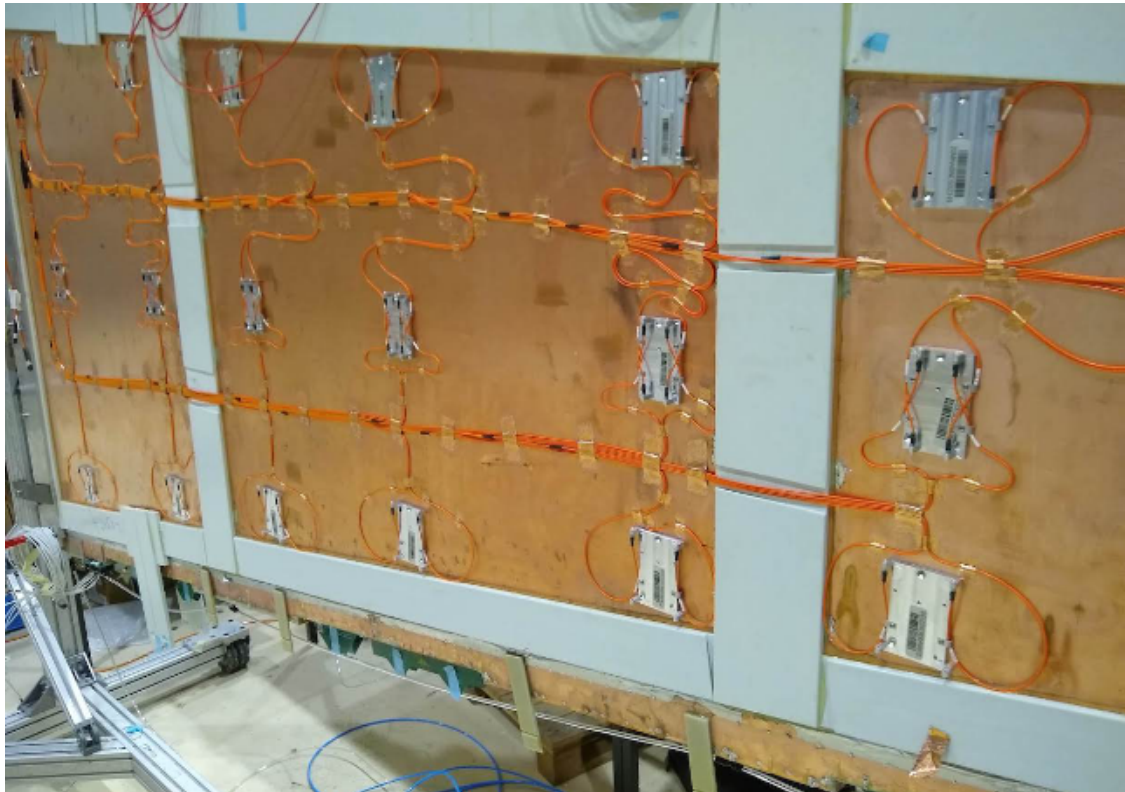


Figure 4.5: An sTGC wedge with alignment platforms (silver) installed on the quadruplet. Optical fibres (orange) are routed to the alignment platforms. Cameras on the frames of the NSWs will record light from the optical fibres to position the alignment platforms in the ATLAS coordinate system.

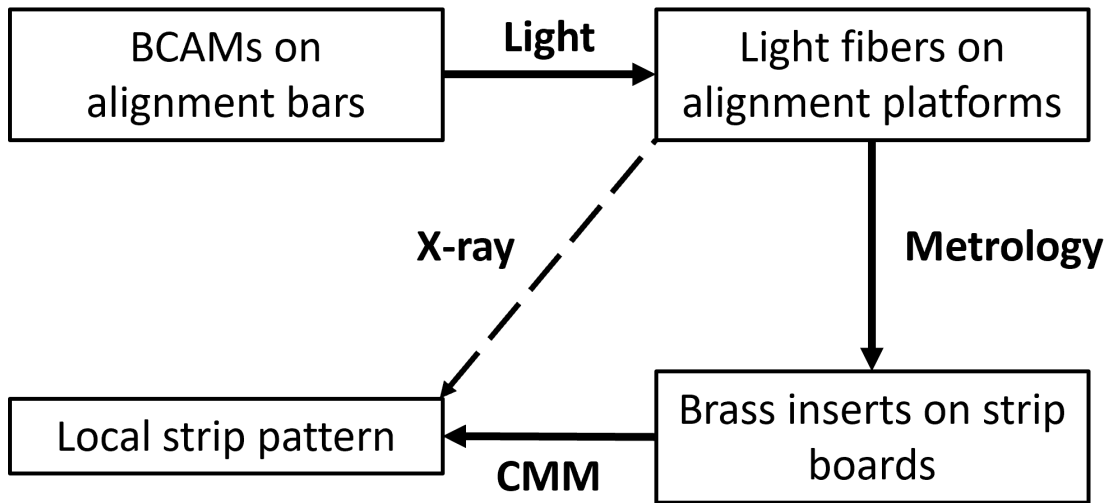


Figure 4.6: How the different elements of the sTGC alignment system relate to one another. The solid arrows denote the planned alignment scheme. The dashed arrow shows the modification being finalized now. This figure was originally designed by Dr. Benoit Lefebvre.

<sup>615</sup> in construction.

<sup>616</sup> Given that the x-ray local offsets can only be measured at positions where the gun can be  
<sup>617</sup> attached and that they are an important part of the alignment scheme, the x-ray method  
<sup>618</sup> needs to be validated. The goal of this thesis is to validate the x-ray local offsets while  
<sup>619</sup> exploring how cosmics data complements and adds to the understanding of strip positions  
<sup>620</sup> and overall alignment.

# 621 Chapter 5

## 622 Using cosmic muons to measure 623 relative strip position offsets

624 At McGill, among other quality and functionality tests, each Canadian-made quadruplet was  
625 characterized with cosmic muons. In this chapter, the experimental setup and how the data  
626 was analyzed to provide relative strip position offsets is presented. The analysis method  
627 was motivated by the how it could be compared to data collected with the x-ray method  
628 (chapter 6) but also stands alone as a characterization of the alignment between strips of  
629 different layers. First, a brief introduction to cosmic rays.

### 630 5.1 Cosmic rays

631 The Earth is being bombarded by particles from the sun, galactic sources and extra galactic  
632 sources – collectively called cosmic rays [19, 11]. Cosmic rays are mostly protons, but also  
633 heavier ions, gamma rays and the term sometimes includes neutrinos. The primary (initial)  
634 cosmic ray interacts with the atmosphere causes electromagnetic and hadronic showers of  
635 particles. Hadronic showers result from the primary cosmic ray interacting strongly with the  
636 target of the atmosphere and the most abundant products are pions. Charge pions mostly  
637 decay to muons (there is a lesser contribution to the muon flux from kaons as well) [59].  
638 Thanks to time dilation extending the muon’s lifetime as measured on Earth, a flux of  
639 approximately 1 muon/cm<sup>2</sup>/ min reaches the ground [11]. Measuring the muon flux and  
640 energy spectrum reveals information about primary cosmic rays [59] which is interesting to  
641 high energy physicists and astrophysicists. The muon flux is also terribly convenient for  
642 testing muon detectors.



Figure 5.1: Cosmic muon hodoscope at McGill University with sTGC quadruplet in the test bench.

## 643 5.2 Experimental setup

644 Cosmic muon characterization was done with a hodoscope, a complete description of which  
 645 can be found in [60]. The quadruplet was placed in the center of the test bench. Above  
 646 and below it was a layer of scintillator-PMT arrays, labeled in figure 5.1. When a cosmic  
 647 muon passed within the acceptance of the hodoscope, at least one scintillator from the top  
 648 array and at least one from the bottom array fired in coincidence. The coincident signal was  
 649 used to trigger the readout of the quadruplet's electrodes using NIM modules. The trigger  
 650 was passed to the front-end electronics attached to the adaptor boards of each layer of the  
 651 quadruplet.

652 Operating the chambers also required gas and high voltage. A pentane-CO<sub>2</sub> mixture was  
 653 mixed and delivered to each sTGC with a gas system designed and made at McGill University.

654 The gas system was controlled by a slow control program, also made in-laboratory [61].  
655 Although gas mixture is flammable, it allows the chambers to operate in high amplification  
656 mode without production of excess photons saturating the signal across many strips because  
657 pentane absorbs a wide energy of photons [56]. To prepare the quadruplets for operation,  
658 CO<sub>2</sub> was flushed through them overnight to remove impurities. Then, five gas volumes of  
659 the pentane-CO<sub>2</sub> mixture was flushed through (approximately 3 hours). High voltage was  
660 provided by CAEN boards.

## 661 5.3 Data acquisition

662 Each sTGC electrode was connected to a channel on a prototype ASIC<sup>1</sup> on the front-end  
663 electronics, attached to the adaptor boards on each layer of a quadruplet. The ASIC ampli-  
664 fied the signal and was set to measure and record the signal peak amplitude from electrodes.  
665 For each trigger, the signal peak amplitude of all channels above threshold was recorded  
666 as an event and stored in a binary file. Channel thresholds were estimated [63] and ad-  
667 justed manually in the configuration/readout software before the start of data acquisition.  
668 There was an exception to the threshold rule: the signals on strips adjacent to a strip above  
669 threshold were also readout using the so-called “neighbour triggering” function of the ASIC.  
670 The quadruplets were held at 3.1 kV for approximately two hours to collect data from 1  
671 million muon triggers.

## 672 5.4 Data preparation

### 673 5.4.1 Cuts on electrode hits

674 Corrupted data is removed while the raw data is being recorded in a binary file. The binary  
675 file is decoded into a usable ROOT [64] tree offline.

676 A hit is defined as a signal recorded from a channel that was above threshold or (in the  
677 case of strips) neighbour triggered. In addition to hits from muons, the quadruplets record  
678 noise from the electronics and  $\delta$ -rays (electrons liberated with sufficient energy to cause more  
679 ionization before acceleration). Therefore, cuts are applied to reduce the number of noise  
680 hits. The edge strips are very noisy, so all strip hits on layers with strip hits on either  
681 edge channel are cut. A default pedestal value is subtracted from the recorded signal peak

---

<sup>1</sup>the VMM3 [62], designed for the MMs and sTGCs of the NSW

682 amplitude of each electrode for a more realistic estimate of the signal amplitude. Also, events  
683 that only have hits on pad electrodes (no strips or wires) were cut because the large area of  
684 the pads made them susceptible to noise.

685 **5.4.2 Clustering and tracking**

686 Many of the high-level characterization metrics require rebuilding muon tracks. For events  
687 passing quality cuts, the  $x$ - and  $y$ -coordinates of the ionization avalanche on each layer are  
688 extracted from the signal on the wires and strips respectively for each event, as is sketched in  
689 figure 5.2. In this work,  $x$  is the coordinate perpendicular to the wires and  $y$  is the coordinate  
690 perpendicular to the strips.

691 The  $x$ -coordinate is taken as the center of the wire group with the maximum peak signal  
692 amplitude, since the wire groups' pitch (36 mm) is larger than the typical charge spreading.  
693 Assuming that the true  $x$ -position of the hit is sampled from a uniform distribution over the  
694 width of the wire group, the uncertainty in the  $x$ -position was given by  $\frac{36}{\sqrt{12}}$  mm = 10 mm [65].

695 The  $y$ -coordinate is taken as the Gaussian mean of the peak signal amplitude distribution  
696 across groups of contiguous strips. The process of grouping contiguous strip hits on a layer is  
697 called clustering, and the resulting group is called a cluster. Figure 5.2 sketches the clustering  
698 process and a sample cluster is shown in figure 5.3. The data acquisition system recorded  
699 the electrode ID of the strip hit and in the clustering process the position of the center  
700 of the strip electrode is calculated based on the nominal quadruplet geometry. Typically,  
701 clusters are built of 3-5 strips. The thickness of the graphite coating over the cathode boards  
702 determined how many strips picked up the ionization image charge. Larger clusters were  
703 more likely caused by  $\delta$ -rays since they spread the cloud of ionization.

704 Events are cut from the analysis if there are two clusters on one layer's set of strips (indicative  
705 of noise). Clusters are cut if the cluster size is lesser than three (which should not happen for  
706 real events thanks to neighbour triggering), and if the cluster size is greater than 25. After  
707 all the cuts on hits and clusters, roughly half as many muon tracks as triggers collected  
708 remain.

709 The uncertainty in the  $y$ -coordinate could have been taken as the fitted cluster mean's  
710 statistical uncertainty; however, after comparing the difference in cluster means for different  
711 fitting algorithms in appendix A.2, 60  $\mu\text{m}$  of uncertainty was assigned.

712 The coordinates of the avalanches' on all layers were used to reconstruct tracks in  $x$  and  $y$   
713 respectively. The tracks were then used to calculate characterization metrics like electrode  
714 efficiency and spatial resolution, the details of which are discussed in [60].

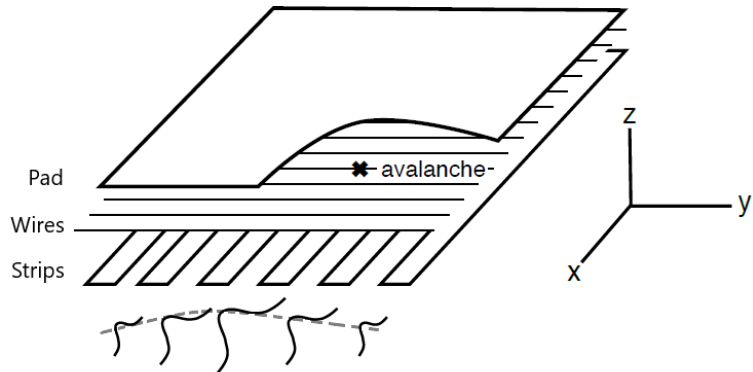


Figure 5.2: A sketch of an sTGC-like detector. The position of the avalanche is extracted from the wires and strips that picked up the avalanche signal. The signals on individual strips are sketched. Clustering was the processs of fitting a Gaussian to the peak value of the signals on individual contiguous strips, as is done in figure 5.3. In this work, the  $x(y)$ -coordinate will always refer to the coordinate perpendicular to the wires (strips) [60, 57].

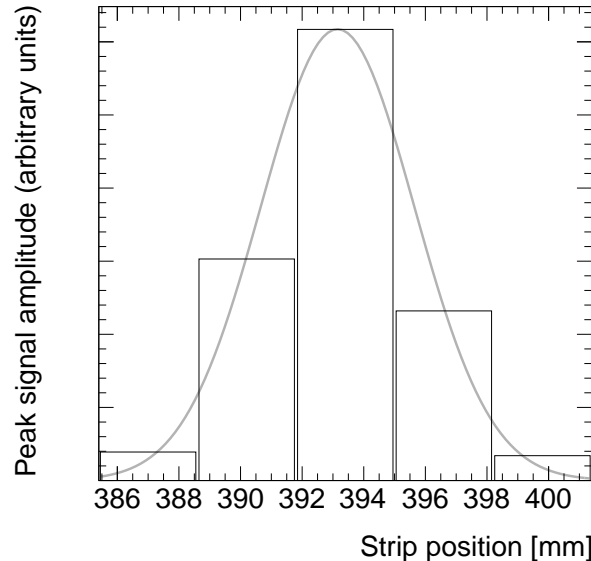


Figure 5.3: A sample cluster resulting from the current picked up on a group of strips after the passing of a muon (presumably). The grey curve is a Gaussian fit.

## 715 5.5 Measuring relative local offsets

716 The offset of a strip from its nominal position can be modeled as a passive transformation.  
717 For each area of a strip layer, the local offset is the shift of the strip pattern in that area with  
718 respect to the nominal geometry. Local offsets systematically change the set of strips nearest  
719 to muons passing through the area. The data preparation software assumes that strips are  
720 in their nominal positions, so the recorded muon  $y$ -position on layer  $i$ ,  $y_i$ , is shifted opposite  
721 to the layer's local offset,  $d_{local,i}$ , by

$$y_i = y_{nom,i} - d_{local,i}, \quad (5.1)$$

722 where  $y_{nom,i}$  is the position of the muon that would have been recorded on layer  $i$  if there  
723 was no local offset. Equation 5.1 ignores other factors that affect the cluster position, like  
724 position resolution. With cosmics data, the local offset is unknown and there was no external  
725 reference to measure  $y_{nom,i}$ . Therefore, only relative local offsets could be calculated.

726 The minimal relative coordinate system uses two reference or fixed layers [60]. The hits  
727 on the two fixed layers were used to create tracks that can be interpolated or extrapolated  
728 (polated) to the other two layers. The set of two fixed layers and the layer polated to are  
729 referred to as a tracking combination. The residual of track  $i$ ,  $\Delta_i$  is defined as,

$$\Delta_i = y_i - y_{track,i}, \quad (5.2)$$

730 where  $y_{track,i}$  is the polated track position. Track residuals are affected by the relative local  
731 offset in the area of each layer's hit. As an example, in figure 5.4, the residual on layer  
732 2 perhaps indicates that layer 2 is offset with respect to layers 1 and 4 in the area of the  
733 track. Of course, a single track residual says nothing of the real relative local offset because  
734 of the limited spatial resolution of the detectors and fake tracks caused by noise or delta  
735 rays. However, the mean of residuals for all tracks in a region will be shifted systematically  
736 by the local offsets between layers [60]. For a quadruplet with nominal geometry, the mean  
737 of residuals should be zero in all regions and for all reference frames, unlike the example  
738 regions in figure 5.5. The value of the mean of residuals is a measure of the relative local  
739 offset of the layer with respect to the two fixed layers.

740 To study the relative local offsets, residual distributions across each strip layer of a quadruplet  
741 for all tracking combinations were assembled and fitted. The residual distributions were  
742 wider for tracking combinations where the extrapolation lever arm was largest, as in the  
743 example distributions shown in figure 5.5. In general, residual means from distributions of  
744 residuals with geometrically less favourable tracking combinations have larger statistical and  
745 systematic uncertainties. The bin size of 200  $\mu\text{m}$  for the distributions shown in figure 5.5 was

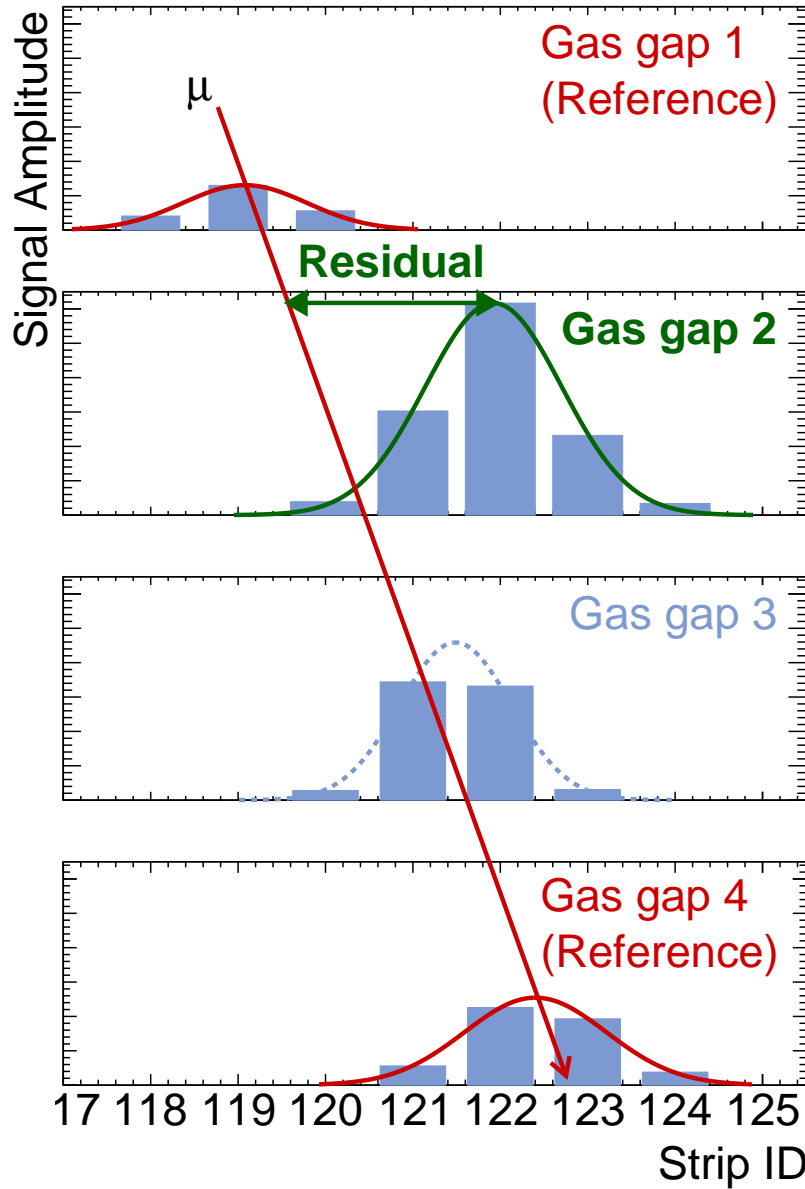
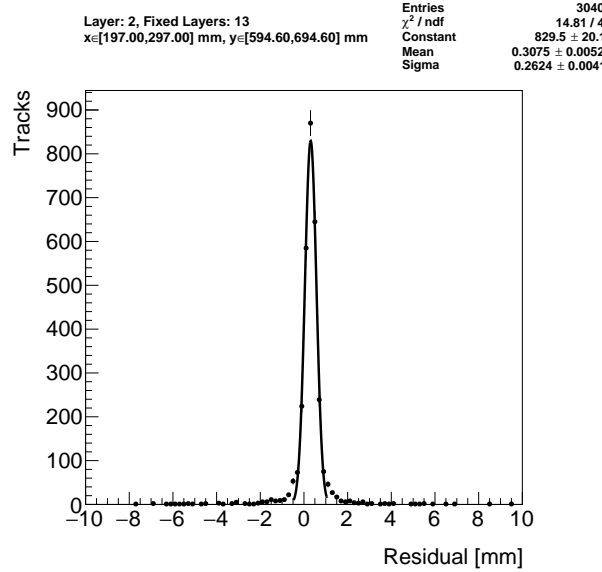
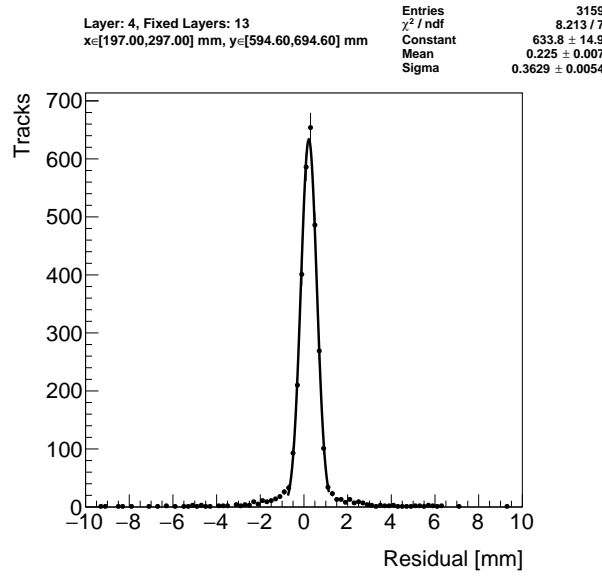


Figure 5.4: Representation of a muon event recorded by an sTGC. The clusters are fit with a Gaussian and the mean is taken as the hit position. A track is built from the chosen reference layers, 1 and 4, and the residual calculated on layer 2. The clusters come from a real muon, but their positions were modified to highlight the residual on layer 2.



(a) Tracks on layer 2, reference layers 1 and 3.



(b) Tracks on layer 4, reference layers 1 and 3.

Figure 5.5: Residual distribution in the region  $x \in [197, 297]$ ,  $y \in [594.6, 694.6]$  mm (100 mm by 100 mm area) for two different tracking combinations. Data from quadruplet QL2.P.11.

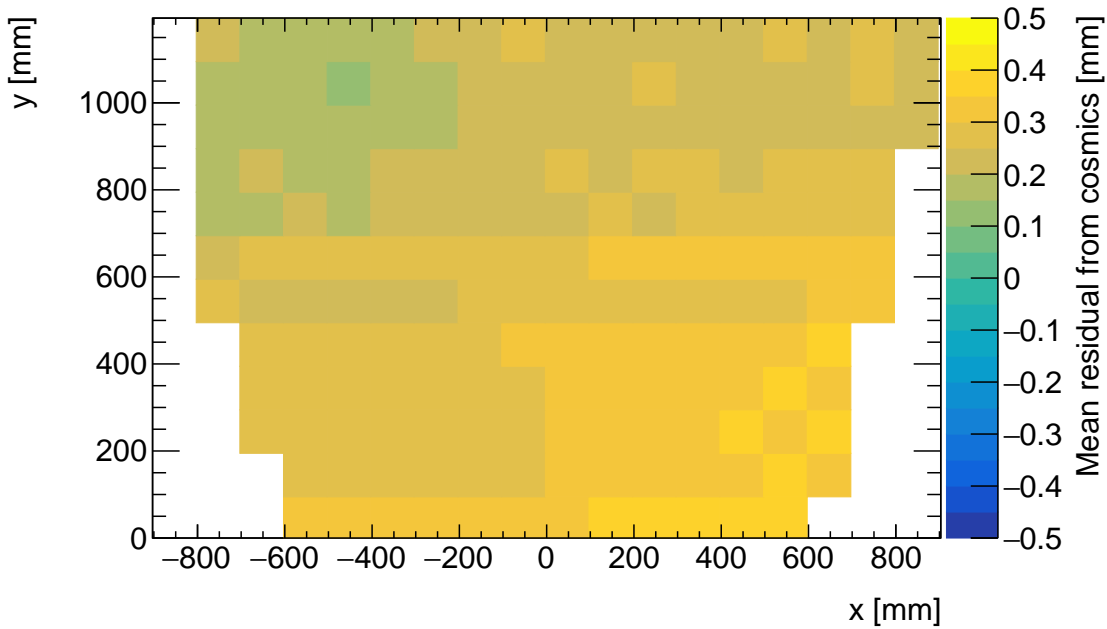
746 chosen based on the uncertainty on residuals calculated from tracks on layer 4 (1) built from  
747 hits on layers 1 and 2 (3 and 4) given a cluster  $y$ -position uncertainty of  $60 \mu\text{m}$  (appendix A.3),  
748 since these tracks yield residuals with the largest uncertainties.

749 A gaussian fit was used to extract the mean of the residual distributions. Theoretically, a  
750 double gaussian distribution is more apt, but for this analysis the gaussian fit was sufficient,  
751 as discussed in appendix C.1.

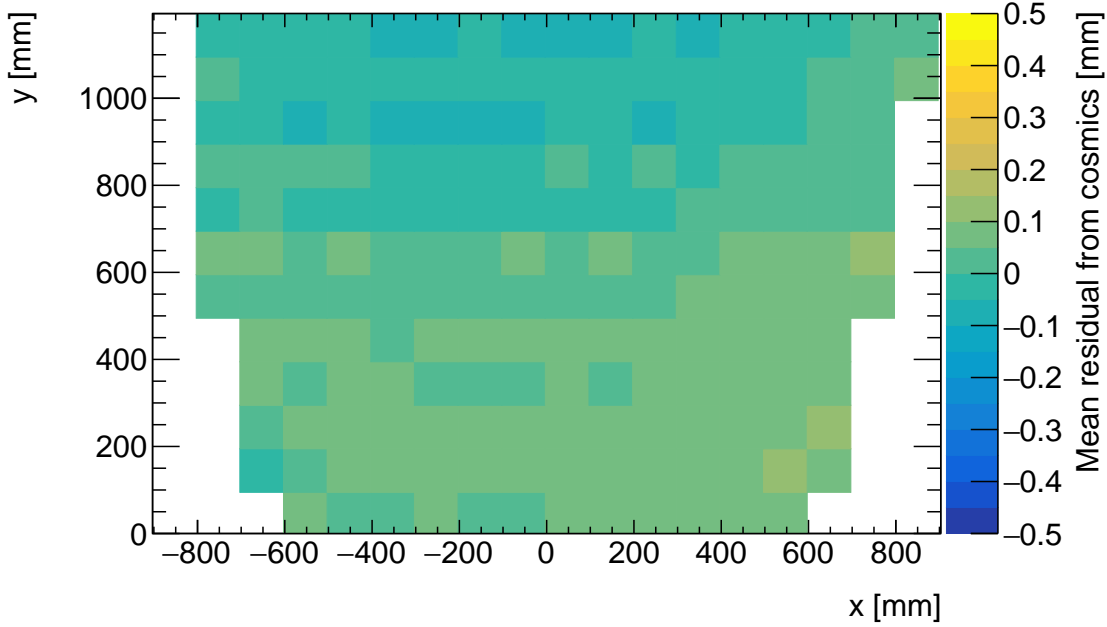
752 The area of the region of interest was 100 mm by 100 mm. The size balanced the amount of  
753 tracks falling in the region of interest to give a small statistical uncertainty on the extracted  
754 mean while being smaller than the order on which local offsets were expected to change  
755 significantly. The change in local offsets over the surface of a layer can be modeled using  
756 global alignment parameters. Using a base alignment model with a global offset and rotation  
757 of each strip layer, “significantly” was defined by the distance in  $x$  that a large but possible  
758 rotation of  $1000 \mu\text{rad}$  would change the local offset by more than  $50 \mu\text{m}$  – half the required  
759 position resolution of the sTGCs [5].

## 760 5.6 Visualizing relative alignment between layers

761 The mean of residuals was plotted across entire strip layers for every tracking combination to  
762 get a picture of the how relative local offsets change over the layers’ surface. Figure 5.6 shows  
763 the mean of residuals on layer 2 with reference layers 1 and 3 for two different quadruplets,  
764 referred to as QL2.P.11 and QL2.P.8, for 100 mm by 100 mm areas across the surface of  
765 layer 2. To understand these plots, realize that the Gaussian mean of the distribution in  
766 figure 5.5a is the entry in area bin  $x \in [197, 297]$ ,  $y \in [594.6, 694.6]$  mm in figure 5.6a.



(a) Mean of residuals of tracks on layer 2, reference layers 1 and 3, for QL2.P.11.



(b) Mean of residuals of tracks on layer 2, reference layers 1 and 3, for QL2.P.8.

Figure 5.6: Mean of residuals in each 100 mm by 100 mm bin over the area of the layer 2 cathode board. The entry in  $x \in [197, 297]$ ,  $y \in [594.6, 694.6]$  mm of figure 5.6a corresponds to the fitted Gaussian means in figures 5.5a. The mean of residuals is an estimate of the local offset of layer 2 with respect to layers 1 and 3.

Many of the residual means are non-zero and change smoothly over the layer, indicating that there are relative local offsets stemming from misalignments between entire strip layers. Given that the residual mean changes with  $x$  in figure 5.6a, there is likely a rotation of layer 2 with respect to layers 1 and 3 on QL2.P.11, combined with an offset of the entire layer. The residual means are smaller in figure 5.6b indicating that QL2.P.8 is less misaligned overall than QL2.P.11; however the relative local offsets range between  $\pm 200 \mu\text{m}$  so they are still significant considering the order on which the chambers must be sensitive to position,  $\sim 100 \mu\text{m}$ .

## 5.7 Systematic uncertainty

The statistical uncertainty on the local residual means was typically around  $10 - 20 \mu\text{m}$ , and appendix B shows that the analysis was not statistically limited by the number of triggers collected for each quadruplet. The systematic uncertainties were more significant.

Systematic uncertainties were assigned per tracking combination as the RMS of the distribution of the difference in local residual means each calculated in a different way. For example, the RMS associated with fitting the local residual distributions with a Gaussian or double Gaussian is  $25 \mu\text{m}$  for the geometrically least favourable tracking combinations. The distribution is shown in appendix C.1. For geometrically similar tracking combinations (like: tracks on layer 1 built from hits on layers 3 and 4, and tracks on layer 4 built from hits on layers 1 and 2), the systematic uncertainty was assigned as the average RMS of both.

Other choices were: whether to use data collected at 2.9 kV or 3.1 kV (both are collected at McGill); what cluster fitting algorithm to use; and whether or not to apply a differential non-linearity (DNL) correction to the cluster  $y$ -positions. A systematic uncertainty was assigned using the method above to account for the effect of each choice and quantify the robustness of the mean of residuals. The reasons for each choice are listed below.

Data taken at 3.1 kV was used over 2.9 kV because the strip and wire tracking efficiency increases with higher voltage [60] (appendix C.2).

The Minuit2 package [66] was used to fit clusters over Guo's method [67] because it provided automatic statistical uncertainty estimates and is the standard fit algorithm of ROOT [64] (appendix C.3).

The DNL correction was not applied because its effect on the residual means was negligible (appendix C.4).

A summary of the systematic uncertainties assigned for each tracking combination is given in table 5.1.

Tracking geometry	Residual distribution fit function <a href="#">(C.1)</a>	Cosmics data collection voltage <a href="#">(C.2)</a>	Cluster fit algorithm <a href="#">(C.3)</a>	Apply DNL correction or not <a href="#">(C.4)</a>	Total
Similar to layer 3, fixed layers 1, 2	0.01	0.04	0.02	0.01	<b>0.05</b>
Similar to layer 4, fixed layers 1, 2	0.03	0.01	0.03	0.01	<b>0.10</b>
Similar to layer 2, fixed layers 1, 3	0.01	0.02	0.01	0.000	<b>0.03</b>
Similar to layer 4, fixed layers 1, 3	0.01	0.04	0.01	0.01	<b>0.04</b>
Similar to layer 2, fixed layers 1, 4	0.01	0.04	0.01	0.01	<b>0.04</b>

Table 5.1: Systematic uncertainty assigned for each analysis option, detailed in appendix [C](#).

800 The uncertainty in each mean of residuals was assigned as the sum in quadrature of the sta-  
801 tistical uncertainty in the mean and the appropriate systematic uncertainty for the tracking  
802 combination.

## 803 5.8 Discussion

804 Cosmics data is being used to calculate relative alignment parameters using two other meth-  
805 ods [60]. A cross-check of this analysis would be to compare their results; however the studies  
806 in appendix C show that the mean cosmics residuals are robust, so the comparison was not  
807 prioritized.

808 Given that the uncertainty in the residual means is lesser than or near to the order of the  
809 required position resolution of the sTGCs (100  $\mu\text{m}$  [5]) they are relevant input for alignment  
810 studies.

811 The relative local offsets as calculated from the mean of residual distributions provide a  
812 complete picture of the relative alignment between detectors planes. In fact, cosmic muon  
813 testing is the only characterization technique where the entire surface of quadruplet layers  
814 can be probed since muons hits are distributed almost uniformly; the CMM [7] and x-ray  
815 methods [8] depend on measurements at reference points, and test beams only have a limited  
816 beam spot [6]. By looking at 2D-histograms of residual means like figure 5.6 for all tracking  
817 combinations, it is easy to identify quadruplets that suffer large relative misalignment since  
818 many residual means differ significantly from zero. Moreover, the pattern in the relative  
819 local offsets can be used to motivate a physical interpretation of misalignments. The relative  
820 local offsets can be used as a reference, cross check, or input in other alignment studies.

821 Relative local offsets cannot be used to position strips in the absolute ATLAS coordinate  
822 system because there was no external reference to measure positions on all layers with re-  
823 spect to. The lack of external reference means that there is not enough information to unfold  
824 relative local offsets into absolute local offsets (with respect to the nominal quadruplet ge-  
825 ometry). As an example, assuming that the residual on layer 2 in figure 5.4 is representative  
826 of the relative local offset, the residual on layer 2 could be caused by the strips on layer 2  
827 being misaligned from nominal, but it could also be caused by strips on layers 1 and 4 being  
828 offset from nominal while the strips on layer 2 are in their nominal positions! Any number  
829 of combinations of local offsets on layers 1, 2 and 4 could produce the residual on layer 2.  
830 Absolute local offsets must be calculated another way.

831 **Chapter 6**

832 **Using x-rays to measure relative strip  
833 position offsets**

834 Local offset measurements were done with the x-ray method. The reader is referred to the  
835 paper describing the x-ray method [8], although some minor changes have been made to the  
836 experimental setup since it was written. The experimental setup described here is current  
837 and was used to collect the data presented in this thesis.

838 **6.1 Experimental setup**

839 The x-ray tests were performed after the quadruplets arrived at CERN, were assembled into  
840 wedges, and alignment platforms installed. Essentially, an x-ray gun was attached to one  
841 of the alignment platforms glued to the surface of the wedge and the x-ray beam profile  
842 recorded by the strips.

843 The wedges were installed on carts that could rotate their surface to a horizontal position. A  
844 mounting platform was installed on top of the alignment platform using a three-ball mount.  
845 The x-ray gun used was an [Amptek Mini-X tube](#). The gun was placed in a brass holder  
846 with built-in 2 mm collimator and 280  $\mu\text{m}$  copper filter. The holder was mounted on one  
847 of five positions on the mounting platform, as shown in figure 6.1. Gun positions were  
848 chosen to avoid wire support structures in the sTGCs that reduce hit efficiency [60] and  
849 boundaries between sets of strips read out by two different ASICs that could each have  
850 different thresholds.

851 As with cosmics data collection, each sTGC also needed gas and high voltage to operate.

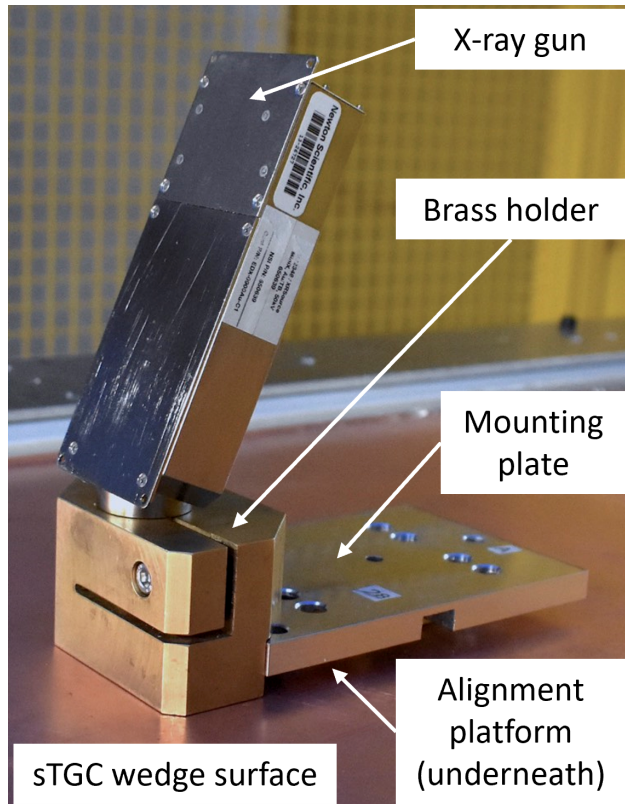


Figure 6.1: The x-ray gun mounted to the alignment platform on the surface of the wedge.  
Adapted from [8].

852 Each layer was operated at 2.925 kV with high voltage from a NIM crate. The chambers  
853 were flushed with CO<sub>2</sub> before and during data collection.  
  
854 The gun produced x-rays with energies under 40 keV with peaks in the 7-15 keV range. The  
855 x-rays mostly interacted with the wedge's copper electrodes and gold-plated tungsten wires  
856 via the photo effect. The resulting photoelectrons caused ionization avalanches that were  
857 picked up by the strips.

## 858 **6.2 Data acquisition**

859 A different version of the same front end electronics, but the same ASIC, as used in cosmics  
860 testing were used for the x-ray testing to amplify the data and measure the peak signal  
861 amplitude. Data was collected for two minutes per gun position with random triggers. A  
862 trigger recorded all signals above threshold. Pad and wire data was not recorded.

## 863 **6.3 Data preparation**

864 Like with cosmics analysis, a default pedestal is subtracted from the signal peak amplitude  
865 on each electrode.  
  
866 Clusters are defined as groups of contiguous strip hits collected within 75 ns. The peak signal  
867 amplitude of each electrode in a cluster is fit with a Gaussian, and the mean of the Gaussian  
868 is taken as the cluster position. Cluster positions are corrected for DNL (see definition in  
869 appendix C.4). Only clusters composed of hits on 3-5 strips were used in the x-ray analysis.  
870 Clusters with signal on more than 5 strips were cut because they were most likely caused by  
871 photoelectrons ejected with enough energy to be  $\delta$ -rays.  
  
872 The x-ray analysis diverges entirely from the cosmics analysis algorithm here because the  
873 x-rays do not leave tracks. The signals picked up by the strips are from photoelectrons  
874 liberated from the metals of the sTGCs, which only travel through one gas volume and are  
875 ejected at all angles. Instead of creating tracks, the cluster position distribution on each  
876 layer is used to define the beam profile. A typical beam profile is shown in figure 6.2.

## 877 **6.4 Measuring local offsets**

878 The mean of the cluster position distribution is taken as the x-ray beam profile center.  
879 The expected center is calculated assuming a wedge with nominal geometry given the gun

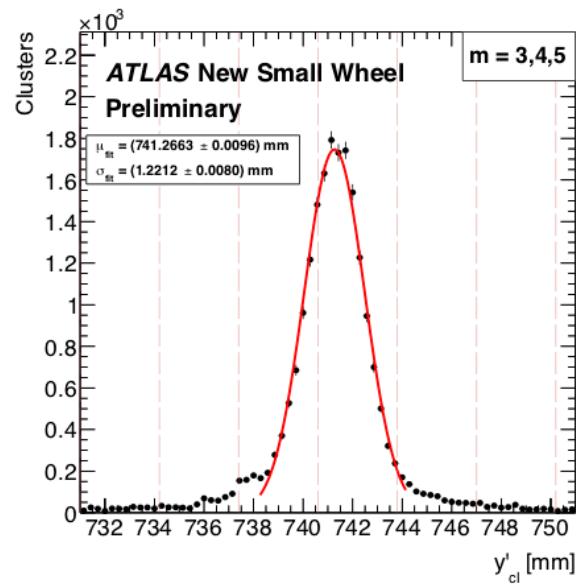


Figure 6.2: Distribution of x-ray cluster mean positions after the analysis cuts and corrections. The strip cluster multiplicity,  $m$ , was limited to 3, 4 and 5. The red curve is a Gaussian fit of the distribution and the pink dashed lines denote the edges of the strips [8].

position, corrected for: the geometry of the brass holder, the positioning and angle of the alignment platforms and the beam angle. The difference between the expected and reconstructed beam profile center is a measure of the local offset. Applying the logic of equation 5.1 to the beam profile, the Gaussian mean of cluster positions on the given layer acts as the recorded position,  $y_i$ , the expected center is  $y_{nom,i}$  and the local offset is  $d_{local,i}$  as before, where  $i$  denotes the layer. Since the position of the alignment platforms will be monitored by the alignment system in ATLAS [5], the position of the strips that should have been at the gun position are shifted by  $d_{local,i}$  and so are known in the ATLAS coordinate system for every position where x-ray data was taken.

The x-ray working group accepted an uncertainty of 120  $\mu\text{m}$  on the beam profile centers. The largest uncertainty comes from the effect of the gun angle, which proved difficult to measure and correct for.

The local offsets are not presented here as the author did not conduct this work. However, the author used the local offsets to calculate relative local offsets.

## 6.5 Measuring relative local offsets

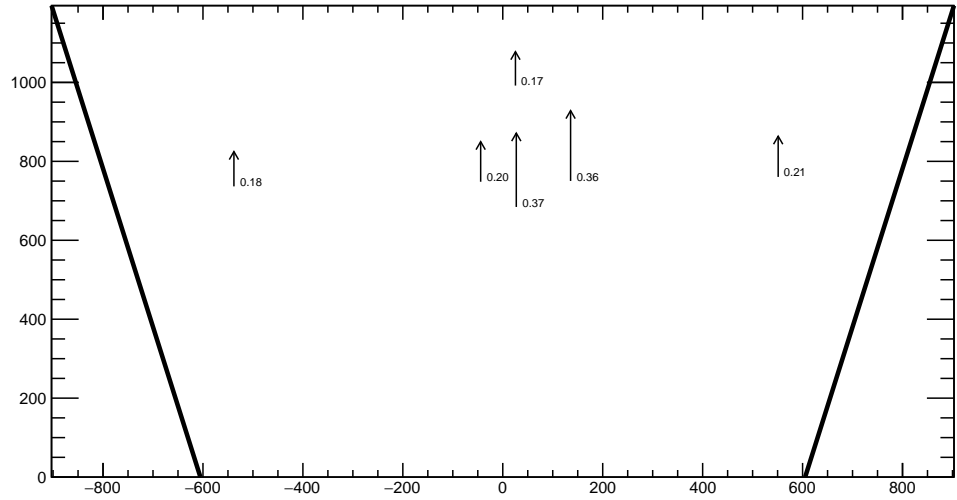
The x-ray local offsets were shown to be correlated with the local offsets calculated from the CMM data, but the CMM data does not include the effect of inter-layer misalignments so the degree of correlation measurable was limited. Cosmics data is affected by inter-layer misalignments. Since the local offsets for x-rays and cosmics data are measured in different coordinate systems, they cannot be compared directly. Bringing the cosmics relative local offsets into an absolute coordinate system is impossible; however, the x-ray local offsets can be brought into a relative coordinate system.

The measured x-ray beam profile centers were systematically affected by local offsets in the same way as the mean cosmics residuals, as modeled by equation 5.1. Therefore, if a 2-layer track is built from the beam profile centers on each layer and the residual calculated on a third layer, that residual should match the local mean cosmics residual. The residual is the difference between the beam profile center on the layer of interest and the polated track position from the beam profile centers recorded on the two fixed layers. The beam profile center on the layer of interest acts as  $y_i$  and the polated track position acts as  $y_{track,i}$  in equation 5.2.

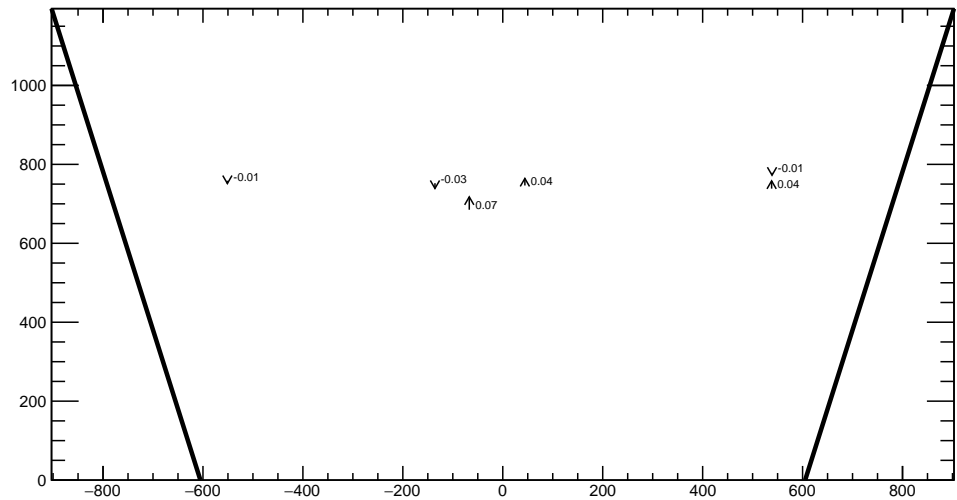
The built track is not an actual track of the x-ray beam. A beam profile center is actually the Gaussian mean of all selected mean cluster positions recorded during the x-ray data taking period, not a single hit of a track. Building an “abstract” track was necessary because

913 the x-rays cause signal in the chamber via the photoeffect so there were not individual “x-  
914 ray tracks” to record. In fact the x-ray data could be collected separately for each layer.  
915 Nonetheless, since the effect of local offsets on the beam profile centers was the same as their  
916 effect on the recorded cosmics cluster positions the difference in algorithm between x-ray  
917 and cosmics analysis was allowed.

918 For each x-ray survey position, the x-ray residual was calculated for all possible tracking  
919 combinations (which required an x-ray beam profile on at least three layers). The x-ray  
920 residuals on layer 2 calculated from the beam profile centers recorded on layers 1 and 3 are  
921 represented as arrows in figure 6.3 as arrows for QL2.P.11 and QL2.P.8. For QL2.P.11, a  
922 negative offset at all x-ray survey positions is clear.



(a) QL2.P.11 x-ray residuals on layer 2, reference layers 1 and 3.



(b) QL2.P.8 x-ray residuals on layer 2, reference layers 1 and 3.

Figure 6.3: The x-ray residuals on layer 2 calculated from the beam profile centers recorded on layers 1 and 3 for QL2.P.11 and QL2.P.8. The arrows originate from the expected position of the beam profile center assuming a nominal geometry, and the lengths are proportional to the calculated x-ray residuals. The tip of the arrow represents where the recorded hit was with respect to where it should have been recorded nominally. The value of the x-ray residuals are annotated in millimeters and have an uncertainty of  $\pm 0.15$  mm.

923 The uncertainty on the x-ray residuals was the error propagated through the tracking, taking  
924 an uncertainty of 120  $\mu\text{m}$  on each beam profile center. The uncertainty on the x-ray residuals  
925 ranged from 0.15 mm to 0.4 mm from the most to least geometrically-favourable tracking  
926 combination. There is no discernible pattern to the x-ray residuals on QL2.P.8 because they  
927 are smaller than the uncertainty. The x-ray residual uncertainties are significantly larger  
928 than the uncertainties on the relative local offsets calculated with cosmics data.

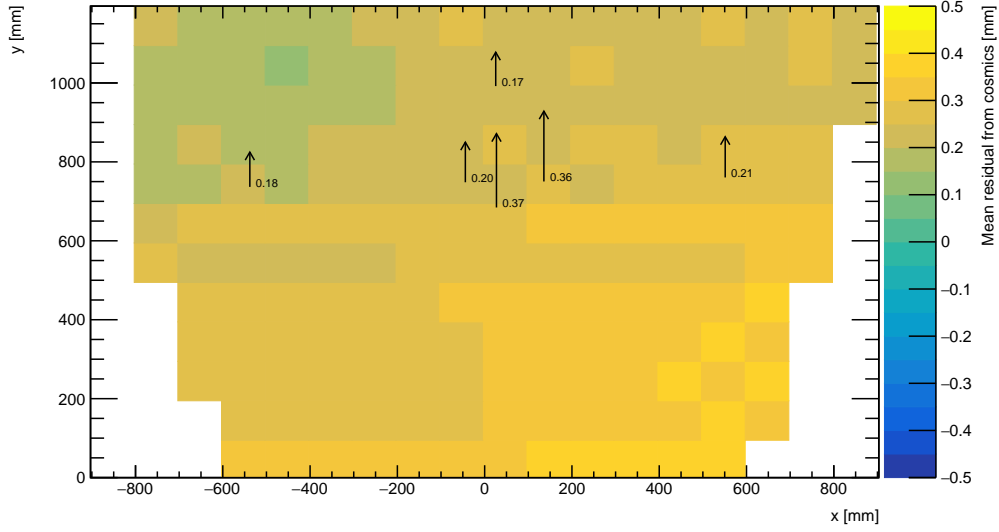
929 **Chapter 7**

930 **Comparing cosmic muon and x-ray  
931 relative strip position offsets**

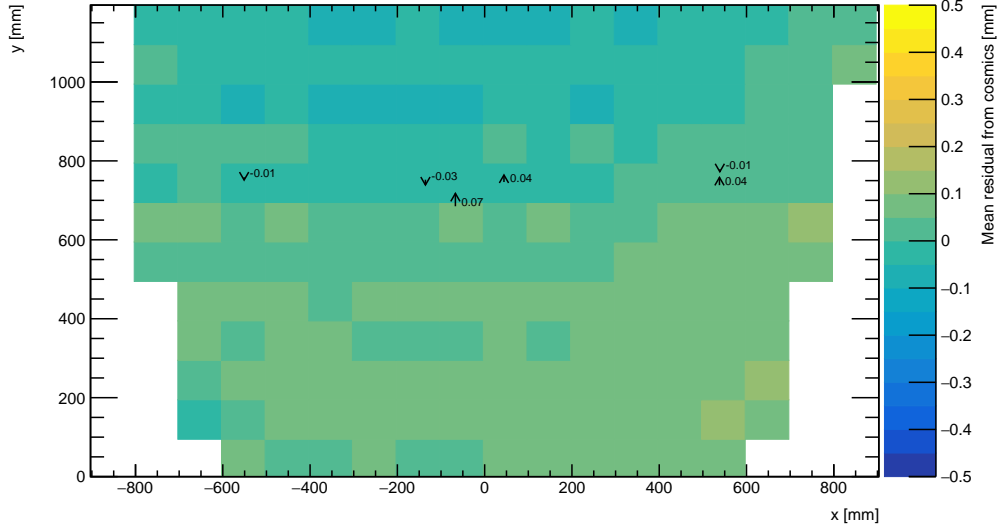
932 The goal was to validate the local offsets extracted from the x-ray data with cosmics data.  
933 The complication was that the x-ray dataset provided absolute local offsets while the cosmics  
934 dataset provided relative local offsets, which could not be compared directly. The solution  
935 was to use the x-ray local offsets to calculate relative local offsets. The x-ray relative local  
936 offset is the x-ray residual reconstructed from an abstract track using the beam profile  
937 centers on each layer as the track hits. The cosmics relative local offset was taken as the  
938 Gaussian mean of muon track residuals in a 100 mm by 100 mm area, referred to as the  
939 mean cosmics residual. Relative local offsets of each type calculated using the same  
940 reference layers are compared for each area where x-ray data is available. The results of the  
941 comparison are presented here.

942 **7.1 Assessing correlation**

943 The 2D visualizations of the mean cosmics and x-ray residuals for tracks on layer 2 with  
944 reference layers 1 and 3 on QL2.P.11 and QL2.P.8 are shown in figure 7.1. Figure 7.1 is a  
945 superposition of figures 5.6 and 6.3.



(a) QL2.P.11 residuals of tracks on layer 2, reference layers 1 and 3.



(b) QL2.P.8 residuals of tracks on layer 2, reference layers 1 and 3.

Figure 7.1: The mean cosmics residuals are shown using colour. The x-ray residuals available at nominal gun positions are drawn as arrows and the value of the residual annotated in millimeters with uncertainty  $\pm 0.15$  mm. The length of the arrows is 500 times the value of the x-ray residual, scaled for visibility. These plots are a superposition of figures 5.6 and 6.3.

946 Figure 7.1a shows that for QL2.P.11 the x-ray residuals are of the same sign and order as  
947 the mean cosmics residuals, as can be seen by comparing the the annotated value of the  
948 x-ray residual to the mean cosmics residual represented by colour; QL2.P.11's mean cosmics  
949 and x-ray residuals are correlated to some degree. For QL2.P.8, the x-ray residuals are of  
950 the right order compared to the mean cosmics residuals, but the correlation is less apparent.  
951 While x-ray residuals do not reveal a pattern across the layer's surface, the mean cosmics  
952 residuals show a structure to the relative local offsets since they vary smoothly over the  
953 surface of layer 2.

954 The comparison of mean cosmics and x-ray residuals was done for several quadruplets for  
955 all tracking combinations (not just layer 2 residuals calculated with fixed layers 1 and 3 like  
956 in figure 7.1). Scatter plots of the x-ray and mean cosmics residuals on QL2.P.11 and -2  
957 for all tracking combinations shown in figures 7.2 and 7.3 reveal the degree of correlation  
958 between the datasets. In the correlation plots, each rectangle is centered on the value of a  
959 mean cosmics and x-ray residual pair calculated with a given tracking combination for every  
960 gun position where data is available; the height and width of the squares are the uncertainty  
961 in the mean cosmics and x-ray residuals respectively. Note that in the scatter plots, the  
962 regions of interest where cosmics tracks are included in the calculation of mean of residuals  
963 are exactly centered on the nominal x-ray beam position, unlike in figure 7.1.

964 The fitted slope and offset in figure 7.2 show that the two QL2.P.11 datasets are correlated.  
965 The large uncertainty on the x-ray residuals set a limit on the sensitivity of the analysis,  
966 for if the absolute value of the x-ray residuals of a quadruplet were smaller than the x-ray  
967 residual uncertainties, no conclusion about the correlation could be drawn, like for QL2.P.8  
968 (figure 7.3). This result is reflected in the small x-ray residuals shown in figure 7.1b that  
969 do not reveal a pattern in the relative local offsets across the surface of layer 2. However,  
970 figure 7.3 shows that the x-ray and mean cosmics residuals are centered around zero, as is  
971 expected for a quadruplet with small relative misalignments between layers.

972 There are three patterns in the residuals on the scatter plot explained by geometry. First,  
973 for both datasets the uncertainty in the extrapolated track residuals were larger than the  
974 interpolated track residuals because of the extrapolation lever arm. For the x-ray residuals,  
975 the effect of the lever arm on the uncertainty was direct since the residual was calculated from  
976 a single abstract track; for the mean cosmics residuals it was the widening of the residual  
977 distribution due to the extrapolation lever arm that increased the uncertainty in the fitted  
978 mean of residuals. Second, residuals calculated through extrapolation tend to be larger  
979 because the extrapolation lever arm can produce more extreme values of the track position  
980 on the layer of interest. Third, the points in figure 7.2 are geometrically correlated (e.g.  
981 they seem to be roughly mirrored around the origin). This is expected since the residuals  
982 calculated using a given set of three layers should be geometrically correlated by the local

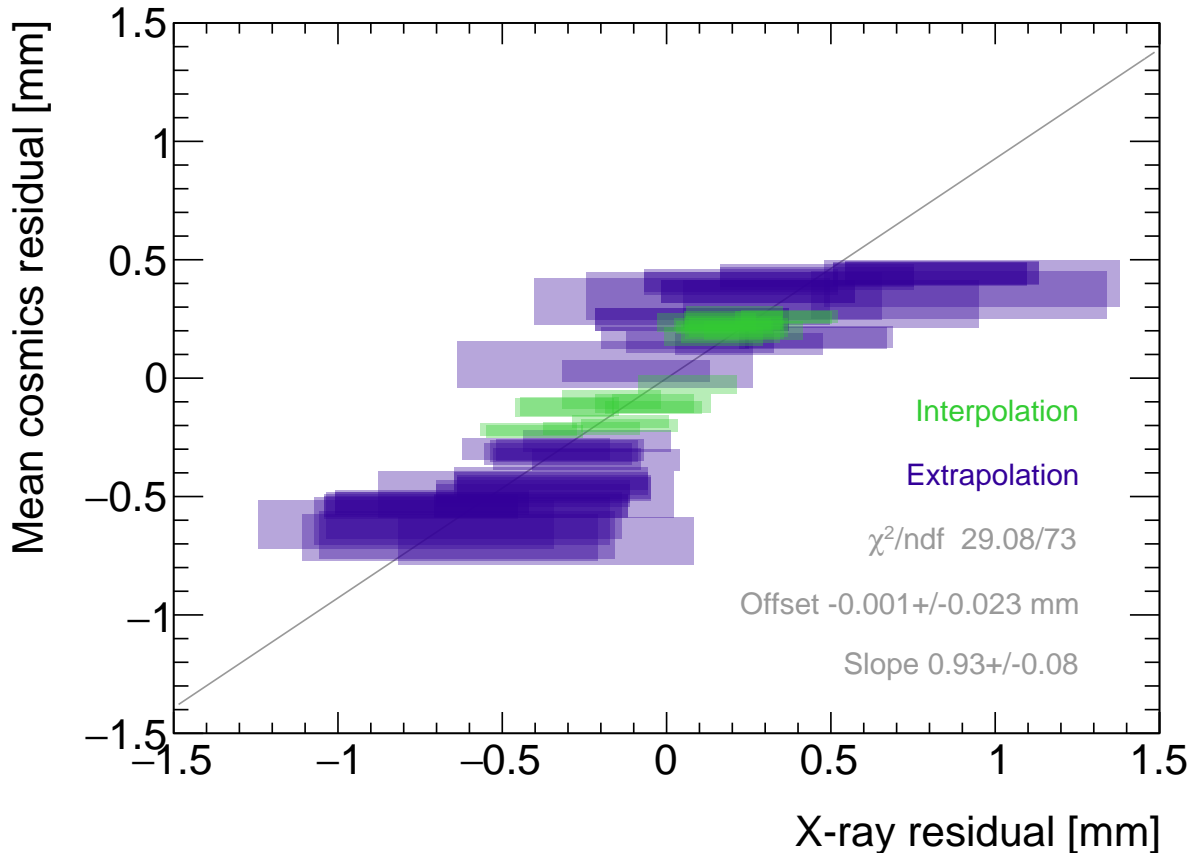


Figure 7.2: Correlation plot between x-ray and mean cosmics residuals for all tracking combinations for QL2.P.11. Each rectangle is centered on an x-ray and mean cosmics residual pair calculated at a given gun position and for a certain tracking combination. The width of the rectangles in  $x$  and  $y$  are the uncertainty in the x-ray and mean cosmics residual respectively. A printer-friendly version of this plot is available in appendix D.

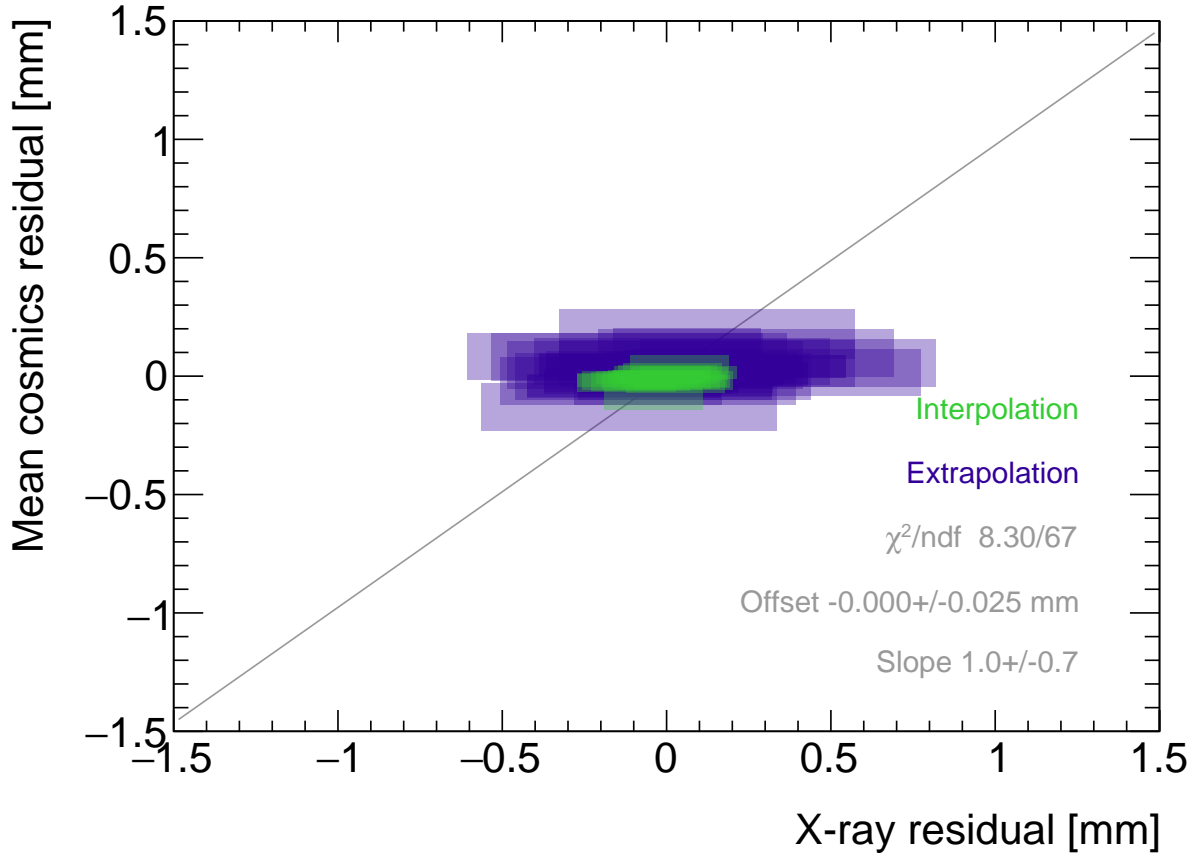


Figure 7.3: Correlation plot between x-ray and mean cosmics residuals for all tracking combinations for quadruplet 2. Each rectangle is centered on an x-ray and mean cosmics residual pair calculated at a given gun position and for a certain tracking combination. The width of the rectangles in  $x$  and  $y$  are the uncertainty in the x-ray and mean cosmics residual respectively. A printer-friendly version of this plot is available in appendix D.

983 offsets on the fixed layers and the layer of interest (the  $d_{local,i}$  on each layer as defined in  
984 equation 5.1).

## 985 7.2 Discussion

986 Several quadruplets were tested for each quadruplet construction geometry built in Canada.  
987 Each quadruplet fell into one of the two categories: residuals large enough to see a correlation,  
988 or residuals too small to see a correlation. Since the x-ray and mean cosmics residuals  
989 were measures of the relative local offsets between the layer and the two reference layers,  
990 quadruplets with the largest relative misalignments had the largest range of residuals. the  
991 correlation plots were an easy visual way to identify quadruplets with large relative misalign-  
992 ments.

993 The most significant limit on measuring the degree of correlation between the x-ray and  
994 mean cosmics residuals was the uncertainty on the x-ray residuals, which stemmed from  
995 the systematic uncertainty of 120  $\mu\text{m}$  in the x-ray beam profile centers used to build the  
996 abstract tracks. For example, in figure 7.3 the uncertainty in the x-ray residuals makes  
997 detecting correlation impossible. The x-ray method was limited primarily by the systematic  
998 uncertainties in the relative alignment of the platforms and the gun, especially the gun angle.

999 The analysis of certain quadruplets was limited by the availability of data. Sometimes,  
1000 less than three layers were surveyed for a given x-ray gun position so no residuals could  
1001 be calculated. Too few x-ray residuals prevented the analysis from detecting a significant  
1002 correlation, should it even be measurable. Often, the analysis of smaller quadruplets (placed  
1003 innermost on the wheel) suffered as a result because they had fewer alignment platforms, and  
1004 hence gun positions, on their surfaces. The analysis was also limited to certain quadruplets.  
1005 The wedges constructed the earliest (typically small wedges) were surveyed when the x-ray  
1006 method was still being designed and so have limited x-ray residuals calculated from beam  
1007 profiles of lower quality. In addition, not all cosmic muon test sites had enough front end  
1008 electronics to collect data on three layers simultaneously, which is the minimum required to  
1009 be able to calculate residuals.

1010 Nonetheless, the comparison of x-ray and cosmics residuals was really to confirm the x-ray  
1011 method's ability to measure local offsets with an independent dataset. The x-ray local offsets  
1012 allow the calculation of relative local offsets that have been correlated to the cosmics relative  
1013 local offsets. Therefore, the analysis of quadruplets with relative local offsets large enough  
1014 to detect a correlation validates the x-ray method's ability to measure local offsets.

1015 The potential of using relative local offsets calculated from cosmics data to study relative  
1016 alignment between sTGC layers stands on its own. For example, although the x-ray relative

1017 local offsets of QL2.P.8 in figure 7.1b do not reveal a pattern, the variation in the cosmics  
1018 relative local offsets do. Identifying the pattern is possible because mean cosmics residuals  
1019 can be calculated across the entire area and are sensitive to smaller relative local offsets since  
1020 their uncertainty is significantly smaller.

1021 The advantage of the x-ray dataset over the cosmics dataset is that absolute local offsets  
1022 are measurable thanks to the reference frame provided by the alignment platforms. This is  
1023 required to measure the position of strips in the ATLAS coordinate system to satisfy the  
1024 NSWs' precision tracking goals. The x-ray local offsets are being used to build an alignment  
1025 model of strips in each quadruplet. It is compelling to imagine using the cosmics relative  
1026 local offsets to improve the model considering their precision and ability to capture effects  
1027 across the entire area of the quadruplet.

1028 **Chapter 8**

1029 **Outlook and summary**

1030 The cosmic muon dataset was used to independently confirm the absolute local offsets mea-  
1031 sured by the x-ray method. The x-ray offsets are being used to complete the sTGC alignment  
1032 scheme of the NSWs: the NSW alignment system monitors the position of alignment plat-  
1033 forms on the surface of sTGC wedges, and the x-ray measurements provide the offsets of  
1034 the strip pattern with respect to each alignment platform. The continuation of this anal-  
1035 ysis is detailed next (section 8.1) before summarizing and considering the larger context  
1036 (section 8.2).

1037 **8.1 Outlook**

1038 Next all quadruplets with suitable cosmics and x-ray data should be surveyed to flag anom-  
1039alous quadruplets (as a first step). If a quadruplet's correlation plot like figure 7.2 or 7.3  
1040 reveals an unexpected correlation or has a large scatter, it would indicate an issue with ei-  
1041ther the cosmics or x-ray data collection to be investigated further. The uncertainty in each  
1042 set of tracking points would inform the interpretation of the anomaly. Then, the quality of  
1043 the correlation should be evaluated over all quadruplets instead of individually.

1044 For now, the correlation for the individual quadruplets tested support the use of the x-ray  
1045 data to build an alignment model [8]. Work on creating an alignment model is ongoing.  
1046 Currently, the algorithm compares the  $y$ -position of a local group of strips at each x-ray gun  
1047 position as measured by the x-ray and CMM methods in a fit to extract a global slope ( $m$ )

1048 and offset ( $b$ ) per layer,  $i$ , where the  $\chi^2$  is given by equation 8.1.

$$\chi^2 = \frac{[dy_{cmm,corr} - dy_{xray}]^2}{\delta dy_{xray}^2 + \delta dy_{cmm,corr}^2}, \quad (8.1)$$

1049

$$dy_{cmm,corr} = y_{cmm} + b_i + m_i x - y_{nom} \quad (8.2)$$

1050 Here,  $dy$  refers to the corrected CMM and x-ray local offsets, and  $\delta dy$  refers to their re-  
1051 spective uncertainties. The CMM measurements were taken before the cathode boards were  
1052 assembled into quadruplets, so alignment parameters for the given layer were extracted from  
1053 the  $\chi^2$  fit by stepping the corrected CMM  $y$ -position towards the x-ray  $y$ -position by adjust-  
1054 ing the layer's slope and offset parameters. The plan is that the alignment parameters will  
1055 be provided to the ATLAS experiment's offline software to reconstruct muon tracks from the  
1056 NSWs' sTGCs. The large uncertainty on the x-ray local offsets (120  $\mu\text{m}$ ) and the sparseness  
1057 of the measurements means that including input from other characterization datasets could  
1058 reduce the uncertainty on the alignment model parameters.

1059 The uncertainty in the mean cosmics residuals was smaller than the desired position reso-  
1060 lution of the sTGCs, so they provide relevant information about strip positions. Moreover,  
1061 they can be calculated over the entire area of the quadruplet instead of at specific posi-  
1062 tions. It would be great to use the cosmics residuals as input to calculate and reduce the  
1063 uncertainty on the alignment parameters. Since mean cosmics residuals can only provide  
1064 relative alignment information, one idea would be to use them to constrain the fit of the  
1065 alignment parameters. In this case, the alignment parameters would need to be fitted on all  
1066 layers at once, and the shifting  $y$ -positions on each layer forced to create an abstracted track  
1067 residual equal to the local mean cosmics residual (within uncertainty) for each x-ray point.  
1068 Or, instead of constraining the fit, it could be penalized if the resulting parameters do not  
1069 result in abstracted track residuals equal to the mean cosmics residuals within uncertainty.  
1070 Some work on using the three datasets at once in a fit has been started.

## 1071 8.2 Summary

1072 The LHC [1] will be at the energy frontier of particle physics for at least the next decade,  
1073 making it a unique tool with which to study particle physics. With the HL-LHC [2], high  
1074 statistics on rare particle physics processes will enable more precise measurements of param-  
1075 eters of the Standard Model and increase the sensitivity to signatures of physics beyond the  
1076 Standard Model [3]. To capitalize on the increased collision rate, the NSWs of the ATLAS  
1077 experiment must be replaced to keep the triggering and tracking performance [5].

1078 Small-strip thin gap chambers are gas ionization chambers optimized for a high rate envi-  
1079 ronment [5]. Using the pad electrodes to define a region of interest makes it possible to get  
1080 track segments of  $\sim 1$  mrad angular resolution quickly, which will be used as input to check  
1081 if a collision originated from the interaction point and should be triggered on or not [5, 54].  
1082 sTGCs are also able to provide better than  $100 \mu\text{m}$  position resolution on each detector plane  
1083 to fulfill precision offline tracking requirements [6].

1084 Ultimately, the positions of the sTGC strip electrodes need to be known in ATLAS to within  
1085  $\sim 100 \mu\text{m}$  so that they can deliver the required position resolution. The ATLAS alignment  
1086 system will position alignment platforms on the surface of the sTGC wedge, and an alignment  
1087 model will be used to position the strips with respect to the alignment platforms [5]. Input  
1088 to the alignment model comes from the datasets used to characterize the quadruplets. The  
1089 x-ray method [8] is used to measure offsets of strips from their nominal position to achieve  
1090 this goal. The alignment model could be built on x-ray data alone, but the sparseness of  
1091 and large uncertainty on the local offsets mean that the alignment model could benefit from  
1092 more input. Comparing the x-ray offsets to the CMM data [7] allows the effect of inter-layer  
1093 misalignments to be isolated and increases the input to the alignment model.

1094 The cosmics dataset was used to confirm the local offsets measured with the x-ray gun. It  
1095 provides relative local offsets between sTGC strip layers. The 2D visualizations of relative  
1096 local offsets allow personnel to quickly identify areas of misaligned strips and make hypothe-  
1097 ses of the physical origin of those misalignments. The correlation seen between the x-ray and  
1098 cosmics relative local offsets in quadruplets with large relative misalignments both confirms  
1099 the validity of the x-ray local offsets and again is a quick way to identify quadruplets with  
1100 large misalignments. Moreover, the mean of track residuals in an area is a robust estimation  
1101 of the relative local offset, as shown by the estimation of systematic uncertainties; the relative  
1102 local offsets for all two-fixed layer reference frames do not change by more than  $100 \mu\text{m}$  given  
1103 variation in data collection conditions and analysis algorithms. The cosmics relative local  
1104 offsets are therefore relevant input for alignment studies and could improve the alignment  
1105 model that will position each strip.

1106 Achieving the required position resolution on each layer of the NSWs in the particle track  
1107 bending plane achieves the design momentum resolution for muons ejected towards the end-  
1108 caps of ATLAS. Muons are important signatures of electroweak and Higgs sector events  
1109 of interest for the ATLAS Collaboration’s future physics goals [5]. Being the second of two  
1110 tracking technologies on the NSWs, an effective alignment model of sTGC quadruplets layers  
1111 is a necessary part of making the NSWs redundant for 10 or more years of recording collisions  
1112 in the High Luminosity era of the LHC.

# <sup>1113</sup> References

- <sup>1114</sup> [1] L Evans and P Bryant. LHC Machine. *Journal of Instrumentation*, 3(S08001), 2008.
- <sup>1115</sup> [2] G Apollinari, I Bejar Alonso, O Bruning, P Fessia, M Lamont, L Rossi, and L Tavian.  
<sup>1116</sup> High-Luminosity Large Hadron Collider (HL-LHC) Technical Design Report V. 0.1.  
<sup>1117</sup> Technical report, CERN, Geneva, September 2017.
- <sup>1118</sup> [3] A Dainese et al. The physics potential of HL-LHC. In *Input to the European Particle  
1119 Physics Strategy Update*, November 2018.
- <sup>1120</sup> [4] The ATLAS Collaboration. The ATLAS Experiment at the CERN Large Hadron Col-  
linder. *Journal of Instrumentation*, 3(08):S08003, 2008.
- <sup>1122</sup> [5] T Kawamoto, S Vlachos, L Pontecorvo, J Dubbert, G Mikenberg, P Iengo, C Dallapic-  
cola, C Amelung, L Levinson, R Richter, and D Lellouch. New Small Wheel Technical  
1123 Design Report. Technical report, Jun 2013. ATLAS New Small Wheel Technical Design  
1124 Report.
- <sup>1125</sup> [6] Angel Abusleme et al. Performance of a Full-Size Small-Strip Thin Gap Chamber Pro-  
totype for the ATLAS New Small Wheel Muon Upgrade. *Nuclear Instruments and  
1127 Methods in Physics Research Section A: Accelerators, Spectrometers, Detectors and As-  
1128 sociated Equipment*, 817:85–92, May 2016. arXiv: 1509.06329.
- <sup>1130</sup> [7] Evan Michael Carlson. *Results of the 2018 ATLAS sTGC test beam and internal strip  
1131 alignment of sTGC detectors*. Thesis, University of Victoria, Victoria, Canada, 2019.  
Accepted: 2019-07-16T17:20:40Z.
- <sup>1133</sup> [8] B. Lefebvre. Precision survey of the readout strips of small-strip Thin Gap Chambers  
1134 using X-rays for the muon spectrometer upgrade of the ATLAS experiment. *Journal of  
1135 Instrumentation*, 15(07):C07013–C07013, July 2020.

- 1136 [9] David J. Griffiths. *Introduction to elementary particles*. Physics textbook. Wiley-VCH,  
 1137 Weinheim, Germany, 2., rev. ed., 5. reprint edition, 2011.
- 1138 [10] Michael Edward Peskin and Daniel V. Schroeder. *An introduction to quantum field  
 1139 theory*. Addison-Wesley Pub. Co, Reading, Massachusetts, 1995.
- 1140 [11] P.A. Zyla et al. Review of Particle Physics. *PTEP*, 2020(8):083C01, 2020.
- 1141 [12] Makoto Kobayashi and Toshihide Maskawa. CP-violation in the renormalizable theory  
 1142 of weak interaction. *Progress of theoretical physics*, 49(2):652–657, February 1973.
- 1143 [13] M. L. Perl, G. S. Abrams, A. M. Boyarski, M. Breidenbach, D. D. Briggs, F. Bulos,  
 1144 W. Chinowsky, J. T. Dakin, G. J. Feldman, C. E. Friedberg, D. Fryberger, G. Goldhaber,  
 1145 G. Hanson, F. B. Heile, B. Jean-Marie, J. A. Kadyk, R. R. Larsen, A. M. Litke, D. Lüke,  
 1146 B. A. Lulu, V. Lüth, D. Lyon, C. C. Morehouse, J. M. Paterson, F. M. Pierre, T. P.  
 1147 Pun, P. A. Rapidis, B. Richter, B. Sadoulet, R. F. Schwitters, W. Tanenbaum, G. H.  
 1148 Trilling, F. Vannucci, J. S. Whitaker, F. C. Winkelmann, and J. E. Wiss. Evidence  
 1149 for Anomalous Lepton Production in  $\{e\}^+ \rightarrow \{e\}^- \{e\}^+ \rightarrow \{e\}^-$  Annihilation. *Physical Review Letters*, 35(22):1489–1492, December 1975. Publisher:  
 1150 American Physical Society.
- 1151 [14] F. Englert and R. Brout. Broken Symmetry and the Mass of Gauge Vector Mesons.  
*Physical Review Letters*, 13(9):321–323, August 1964. Publisher: American Physical  
 1152 Society.
- 1153 [15] P. W. Higgs. Broken symmetries, massless particles and gauge fields. *Physics Letters*,  
 1154 12(2):132–133, September 1964.
- 1155 [16] David Galbraith and Carsten Burgard. UX: Standard Model of the Standard Model,  
 1156 November 2013.
- 1157 [17] Carlos A. Bertulani. *Nuclear physics in a nutshell*. In a nutshell. Princeton University  
 1158 Press, Princeton, N.J, 2007. OCLC: ocm85690422.
- 1159 [18] Bradley W. Carroll and Dale A. Ostlie. *An introduction to modern astrophysics*. Pearson  
 1160 Addison-Wesley, San Francisco, 2nd ed edition, 2007. OCLC: ocm69020924.
- 1161 [19] Mirko Boezio and Emiliano Mocchiutti. Chemical composition of galactic cosmic rays  
 1162 with space experiments. *Astroparticle Physics*, 39-40:95–108, December 2012.
- 1163 [20] B. Aharmim et al. Combined analysis of all three phases of solar neutrino data from  
 1164 the sudbury neutrino observatory. *Phys. Rev. C*, 88:025501, Aug 2013.

- 1167 [21] B. Pontecorvo. Neutrino Experiments and the Problem of Conservation of Leptonic  
 1168 Charge. *Zh. Eksp. Teor. Fiz.*, 53:1717–1725, 1967.
- 1169 [22] S. M. Bilenky and S. T. Petcov. Massive neutrinos and neutrino oscillations. *Reviews*  
 1170 *of Modern Physics*, 59(3):671–754, July 1987.
- 1171 [23] Bing-Lin Young. A survey of dark matter and related topics in cosmology. *Frontiers of*  
 1172 *Physics*, 12(2):121201, April 2017.
- 1173 [24] Carlos Muñoz. Dark matter detection in the light of recent experimental results. *International*  
 1174 *Journal of Modern Physics A*, 19(19):3093–3169, July 2004.
- 1175 [25] Gerard Jungman, Marc Kamionkowski, and Kim Griest. Supersymmetric dark matter.  
 1176 *Physics Reports*, 267(5):195–373, March 1996.
- 1177 [26] G. Arnison et al. Experimental observation of isolated large transverse energy elec-  
 1178 trons with associated missing energy at  $s=540$  GeV. *Physics Letters B*, 122(1):103–116,  
 1179 February 1983.
- 1180 [27] M. Banner et al. Observation of single isolated electrons of high transverse momentum  
 1181 in events with missing transverse energy at the CERN pp collider. *Physics Letters B*,  
 1182 122(5):476–485, March 1983.
- 1183 [28] G. Arnison et al. Experimental observation of lepton pairs of invariant mass around 95  
 1184 GeV/c<sup>2</sup> at the CERN SPS collider. *Physics Letters B*, 126(5):398–410, July 1983.
- 1185 [29] P. Bagnaia et al. Evidence for  $Z \rightarrow e^+e^-$  at the CERN pp collider. *Physics Letters B*,  
 1186 129(1):130–140, 1983.
- 1187 [30] CDF Collaboration. Observation of Top Quark Production in  
 1188  $\overline{p}p$  Collisions with the Collider Detector at Fermilab. *Physical Review Letters*, 74(14):2626–2631, April 1995. Publisher: American  
 1189 Physical Society.
- 1190 [31] D0 Collaboration. Observation of the Top Quark. *Physical Review Letters*, 74(14):2632–  
 1191 2637, April 1995. Publisher: American Physical Society.
- 1192 [32] The ATLAS Collaboration. Observation of a new particle in the search for the Standard  
 1193 Model Higgs boson with the ATLAS detector at the LHC. *Physics Letters B*, 716(1):1–  
 1194 29, September 2012. arXiv: 1207.7214.

- 1196 [33] The CMS Collaboration. Observation of a new boson at a mass of 125 GeV with the  
1197 CMS experiment at the LHC. *Physics Letters B*, 716(1):30–61, September 2012. arXiv:  
1198 1207.7235.
- 1199 [34] Standard Model Summary Plots June 2021.
- 1200 [35] Oliver Sim Brüning, Paul Collier, P Lebrun, Stephen Myers, Ranko Ostojic, John Poole,  
1201 and Paul Proudlock. *LHC Design Report*. CERN Yellow Reports: Monographs. Geneva,  
1202 2004.
- 1203 [36] ATLAS luminosity public results run-1, March 2011.
- 1204 [37] ATLAS luminosity public results run-2, July 2015.
- 1205 [38] The European Strategy for Particle Physics. Technical Report CERN/2685, CERN,  
1206 2006. Adopted by the CERN council at a special session at ministerial level in Lisbon  
1207 in 2006.
- 1208 [39] HiLumi HL-LHC Project. LHC/HL-LHC plan (last update january 2021). <https://hilumilhc.web.cern.ch/content/hl-lhc-project>, last accessed on 2021-09-09.
- 1209
- 1210 [40] M. Cepeda et al. Report from Working Group 2: Higgs Physics at the HL-LHC and  
1211 HE-LHC. *CERN Yellow Rep. Monogr.*, 7:221–584. 364 p, Dec 2018.
- 1212 [41] ATLAS inner detector : Technical Design Report, 1. Technical Report CERN-LHCC-  
1213 97-016, CERN, 1997. ISBN: 9789290831020 Publication Title: CERN Document Server.
- 1214 [42] L. Rossi, S. Haywood, A. Romanouk, and R. Nickerson. ATLAS inner detector : Tech-  
1215 nical Design Report, 2. Technical Report CERN-LHCC-97-017, CERN, 1997. ISBN:  
1216 9789290831037 Publication Title: CERN Document Server.
- 1217 [43] Claus Grupen, Boris A Shwartz, and Helmuth Spieler. *Particle detectors*. Cambridge  
1218 University Press, Cambridge, UK; New York, 2008. OCLC: 1105536566.
- 1219 [44] ATLAS liquid-argon calorimeter : Technical Design Report. Technical Report CERN-  
1220 LHCC-96-041, CERN, 1996. ISBN: 9789290830900 Publication Title: CERN Document  
1221 Server.
- 1222 [45] ATLAS tile calorimeter : Technical Design Report. Technical Report CERN-LHCC-96-  
1223 042, CERN, 1996. ISBN: 9789290830917 Publication Title: CERN Document Server.
- 1224 [46] ATLAS Collaboration. ATLAS Muon Spectrometer: Technical Design Report. Techni-  
1225 cal Report CERN-LHCC-97-022, CERN, Geneva, 1997.

- 1226 [47] ATLAS magnet system : Technical Design Report, 1. Technical Report CERN-LHCC-  
1227 97-018, CERN, 1997. ISBN: 9789290831044 Publication Title: CERN Document Server.
- 1228 [48] ATLAS Collaboration. Performance of the ATLAS muon trigger in pp collisions at  
1229  $\sqrt{s}=8$  TeV. *The European Physical Journal C*, 75(3):120, March 2015. arXiv:  
1230 1408.3179.
- 1231 [49] S. Aefsky, C. Amelung, J. Bensinger, C. Blocker, A. Dushkin, M. Gardner, K. Hashemi,  
1232 E. Henry, B. Kaplan, P. Keselman, M. Ketchum, U. Landgraf, A. Ostapchuk, J. Roth-  
1233 berg, A. Schricker, N. Skvorodnev, and H. Wellenstein. The Optical Alignment System  
1234 of the ATLAS Muon Spectrometer Endcaps. *Journal of Instrumentation*, 3(11):P11005–  
1235 P11005, November 2008. Publisher: IOP Publishing.
- 1236 [50] ATLAS level-1 trigger : Technical Design Report. Technical Report CERN-LHCC-98-  
1237 014, CERN, 1998. ISBN: 9789290831280 Publication Title: CERN Document Server.
- 1238 [51] A Ruiz Martínez and. The run-2 ATLAS trigger system. *Journal of Physics: Conference  
1239 Series*, 762:012003, oct 2016.
- 1240 [52] Technical Design Report for the Phase-II Upgrade of the ATLAS TDAQ System. Tech-  
1241 nical report, CERN, Geneva, Sep 2017.
- 1242 [53] Marzio Nessi, Markus Nordberg, Peter Jenni, and Kenway Smith. ATLAS high-level  
1243 trigger, data-acquisition and controls : Technical Design Report. Technical Report  
1244 CERN-LHCC-2003-022, CERN, 2003. Publication Title: CERN Document Server.
- 1245 [54] E. Perez Codina. Small-strip Thin Gap Chambers for the muon spectrometer upgrade of  
1246 the ATLAS experiment. *Nuclear Instruments and Methods in Physics Research Section  
1247 A: Accelerators, Spectrometers, Detectors and Associated Equipment*, 824:559–561, July  
1248 2016.
- 1249 [55] John Townsend. *Electricity in gases*. Clarendon Press, Oxford, 1915.
- 1250 [56] S. Majewski, G. Charpak, A. Breskin, and G. Mikenberg. A thin multiwire chamber  
1251 operating in the high multiplication mode. *Nuclear Instruments and Methods*, 217:265–  
1252 271, 1983.
- 1253 [57] E. Gatti, A. Longoni, H. Okuno, and P. Semenza. Optimum geometry for strip cathodes  
1254 or grids in MWPC for avalanche localization along the anode wires. *Nuclear Instruments  
1255 and Methods*, 163(1):83–92, July 1979.

- 1256 [58] G. Battistoni, P. Campana, V. Chiarella, U. Dotti, E. Iarocci, and G. Nicoletti. Resistive cathode transparency. *Nuclear Instruments and Methods in Physics Research*,  
 1257 202(3):459–464, November 1982.
- 1259 [59] P. K. F. Grieder. *Cosmic rays at Earth: researcher's reference manual and data book*.  
 1260 Elsevier Science Ltd, Amsterdam, 1st ed edition, 2001.
- 1261 [60] Benoit Lefebvre. *Characterization studies of small-strip Thin Gap Chambers for the ATLAS Upgrade*. PhD Dissertation, McGill University, Montreal, Canada, 2018.
- 1263 [61] R. Keyes, K.A. Johnson, L. Pepin, F. Léger, C. Qin, S. Webster, A. Robichaud-Véronneau, C. Bélanger-Champagne, B. Lefebvre, S.H. Robertson, A. Warburton, B. Vachon, and F. Corriveau. Development and characterization of a gas system and its associated slow-control system for an ATLAS small-strip thin gap chamber testing facility. *Journal of Instrumentation*, 12(04):P04027–P04027, April 2017.
- 1268 [62] George Iakovidis. VMM3, an ASIC for Micropattern Detectors. In *Proceedings of Science*, page 5, Philadelphia, 2017.
- 1270 [63] Bohan Chen. *Calibration Studies of the Front-End Electronics for the ATLAS New Small Wheel Project*. PhD thesis, McGill University, Montreal, Canada, 2019.
- 1272 [64] R. Brun and F. Rademakers. ROOT: An object oriented data analysis framework. *Nucl. Instrum. Meth. A*, 389:81–86, 1997. See also "ROOT" [software], Release 6.18/02, 23/08/2019, (<https://zenodo.org/record/3895860#.YVJW6n0pCHs>).
- 1275 [65] Fabio Sauli. Principles of operation of multiwire proportional and drift chambers. In *Cern Yellow Reports: Monographs*, page 92 p, Geneva, 1977. CERN, CERN. CERN, Geneva, 1975 - 1976.
- 1278 [66] M. Hatlo, F. James, P. Mato, L. Moneta, M. Winkler, and A. Zsenei. Developments of mathematical software libraries for the LHC experiments. *IEEE Trans. Nucl. Sci.*, 52:2818–2822, 2005.
- 1281 [67] Hongwei Guo. A Simple Algorithm for Fitting a Gaussian Function [DSP Tips and Tricks]. *IEEE Signal Processing Magazine*, 28(5):134–137, September 2011.
- 1283 [68] Ichita Endo, Tatsuo Kawamoto, Yoshinari Mizuno, Takashi Ohsugi, Takashi Taniguchi, and Tohru Takeshita. Systematic shifts of evaluated charge centroid for the cathode read-out multiwire proportional chamber. *Nuclear Instruments and Methods in Physics Research*, 188(1):51–58, September 1981.

- 1287 [69] Bernd Stelzer. The New Small Wheel Upgrade Project of the ATLAS Experiment.  
1288     *Nuclear and Particle Physics Proceedings*, 273-275:1160–1165, April 2016.
- 1289 [70] Xiao Zhao, Wenlong Li, Dengfeng Zhang, Changyu Li, Han Li, Shengquan Liu, Peng  
1290     Miao, Yanyan Du, Yanyun Duan, and Chengguang Zhu. Cosmic test of sTGC detector  
1291     prototype made in China for ATLAS experiment upgrade. *Nuclear Instruments and  
1292     Methods in Physics Research Section A: Accelerators, Spectrometers, Detectors and  
1293     Associated Equipment*, 927:257–261, May 2019.
- 1294 [71] Manfred Krammer. Upgrade Programs of the LHC Experiment, November 2017.
- 1295 [72] Benoit Lefebvre. stgc\_as\_built\_fit.
- 1296 [73] Benoit Lefebvre. tgc\_analysis.
- 1297 [74] The ATLAS Collaboration. Athena.
- 1298 [75] Lia Formenti. cosmics\_xray\_correlation.
- 1299 [76] Siyuan Sun. sTGC\_readout\_sw.
- 1300 [77] G Brianti. Large Hadron Collider in the LEP Tunnel. In *Proceedings of the ECFA-CERN  
1301     Workshop*, volume 1, page 352, Lausanne and Geneva, March 1984.
- 1302 [78] Letter of Intent for the Phase-I Upgrade of the ATLAS Experiment. Technical Report  
1303     CERN-LHCC-2011-012. LHCC-I-020, CERN, Geneva, November 2011.
- 1304 [79] ATLAS: letter of intent for a general-purpose pp experiment at the large hadron collider  
1305     at CERN. Technical Report CERN-LHCC-92-004, CERN, Geneva, 1992.
- 1306 [80] The ATLAS Collaboration. Technical Design Report for the Phase-I Upgrade of the  
1307     ATLAS TDAQ System. Technical report, Sep 2013. Final version presented to December  
1308     2013 LHCC.
- 1309 [81] Howard Georgi and S. L. Glashow. Unity of all elementary-particle forces. *Phys. Rev.  
1310     Lett.*, 32:438–441, Feb 1974.
- 1311 [82] Luca Lista. *Statistical Methods for Data Analysis in Particle Physics*, volume 941 of  
1312     *Lecture Notes in Physics*. Springer International Publishing, Cham, 2017.
- 1313 [83] K. Kodama et al. Detection and analysis of tau neutrino interactions in DONUT  
1314     emulsion target. *Nucl. Instrum. Meth. A*, 493:45–66, 2002.

<sup>1315</sup> APPENDICES

1316 **Appendix A**

1317 **Uncertainty in cluster positions**

1318 **A.1 Cluster definition**

1319 A cluster is a series of contiguous strip channels on a layer with non-zero amplitude, all  
1320 part of the same trigger and having the same event number [60]. Clusters result from the  
1321 drift of ionization products generate in the ionization avalanche caused by a muon [55]. The  
1322 peak-detector-output (PDO) of the signal on each strip of a cluster is fit with a Gaussian.  
1323 The y-position of a particle as it passed through the layer is mean of the cluster, referred to  
1324 here as the hit position.

1325 **A.2 Effect of fit algorithm on cluster mean**

1326 The clusters were fit with Guo's method [67] and Minuit2 for ROOT [66]. The difference in  
1327 cluster means between the two algorithms is shown in figure A.1.  
1328 The RMS of the distribution in figure A.1 is  $57 \mu\text{m}$ , which is much larger than the statistical  
1329 uncertainty in the mean for the Minuit2 algorithm, which peaks around  $7 \mu\text{m}$ . An RMS of  
1330  $60 \mu\text{m}$  is common for data taken with most quadruplets at 3.1 kV. Therefore, the uncertainty  
1331 in the y-hit positions is assigned  $60 \mu\text{m}$ .

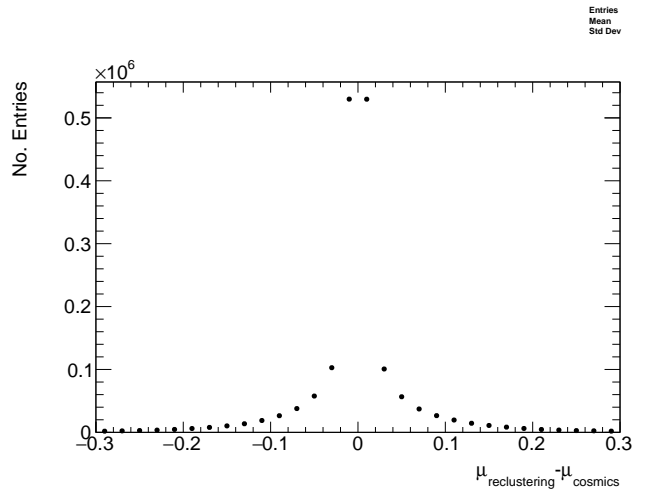


Figure A.1: The difference between cluster means calculated with Guo's method [67] in `tgc_analysis/CosmicsAnalysis` and `Minuit2` for `ROOT` [66] in `strip_position_analysis/ReClustering` for data collected with QL2.P.8 at 3.1 kV.

<sub>1332</sub> **A.3 Effect of uncertainty in cluster mean on track residuals**

<sub>1333</sub>

<sub>1334</sub> The uncertainty assigned to the hit position affected the uncertainty in the extrapolated/interpolated  
<sub>1335</sub> position of the track, and in the residuals. The bin size of the residual distributions was set  
<sub>1336</sub> to 200  $\mu\text{m}$  because that was the uncertainty in the residuals calculated from the tracks with  
<sub>1337</sub> the least favourable geometry (like tracks built from hits on layers 1 and 2 and extrapolated  
<sub>1338</sub> to layer 4).

<sub>1339</sub> **Appendix B**

<sub>1340</sub> **Study of cosmics for alignment  
1341 analysis statistical uncertainty**

<sub>1342</sub> Typically, one million triggers (cosmic muon events, noise, photons and  $\delta$ -rays) were collected  
<sub>1343</sub> for each Canadian quadruplet at McGill University, resulting in roughly half the number of  
<sub>1344</sub> viable tracks after cuts. For QS3.P.18, 3.5 million triggers were collected. To gauge the  
<sub>1345</sub> sensitivity of the analysis to the available statistics, partitions of this data with each with  
<sub>1346</sub> a different number of triggers were analyzed separately. Ultimately, the quantity of interest  
<sub>1347</sub> was the gaussian mean of the residual distribution in regions of interest, so the peak in the  
<sub>1348</sub> distribution of the statistical uncertainty in the residual means for each area of interest for  
<sub>1349</sub> a specific tracking combination was used to gauge the quality of the analysis. How the peak  
<sub>1350</sub> in the residual mean uncertainty distribution changes with the number of triggers is shown  
<sub>1351</sub> in figure for tracks on layer 1 built from layers 3 and 4 [B.1](#).

<sub>1352</sub> The uncertainty is already around 20  $\mu\text{m}$  at 1 million triggers, suitable for distinguishing  
<sub>1353</sub> differences in offsets of order 50  $\mu\text{m}$  as required. Although increased statistics could decrease  
<sub>1354</sub> the statistical uncertainty, it is not required for the goals of this analysis. Moreoever, the  
<sub>1355</sub> systematic uncertainty is around 50  $\mu\text{m}$  and the systematic uncertainty on the x-ray residuals  
<sub>1356</sub> is 150  $\mu\text{m}$  so the statistical uncertainty of 20  $\mu\text{m}$  is nearly negligible.

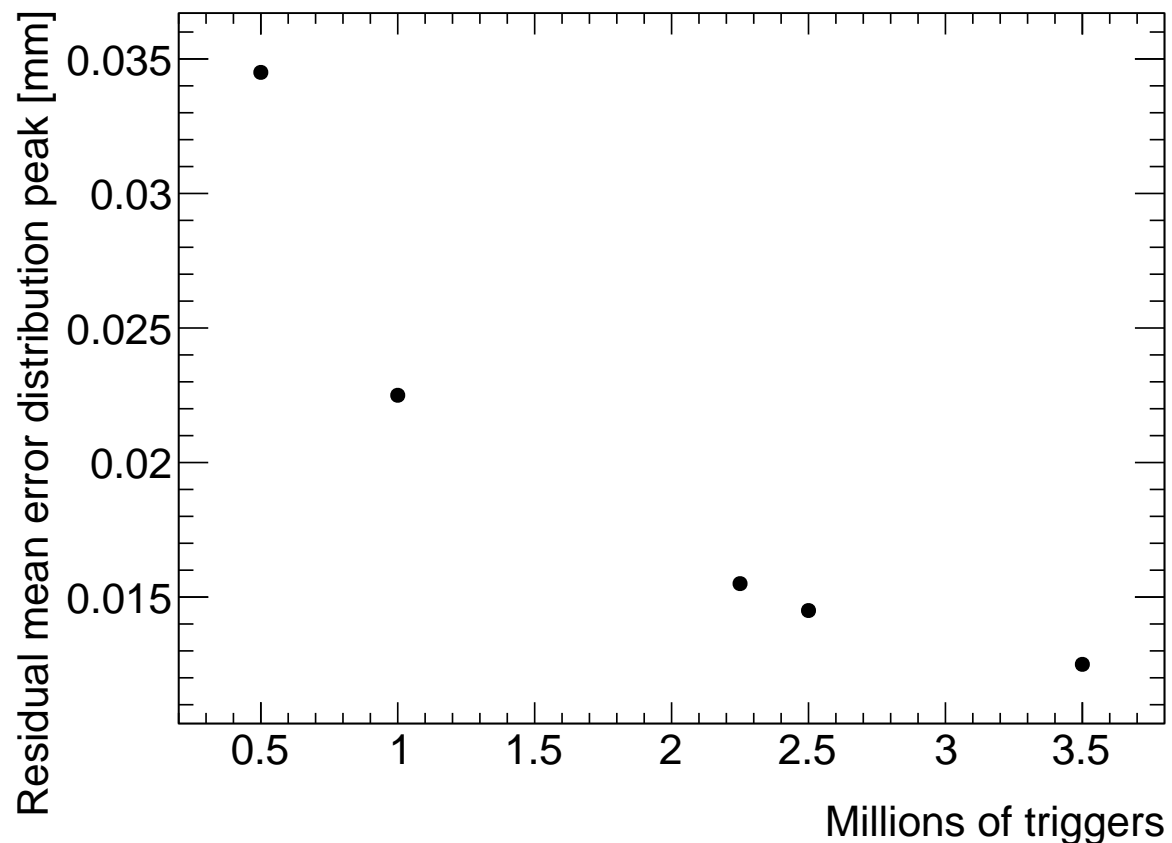


Figure B.1: How the peak of the distributions of uncertainties in the residual means in regions of interest for tracks on layer 1 built from layers 3 and 4 changed with the number of triggers used in the analysis. The distribution falls off as  $\frac{1}{\sqrt{N}}$  as expected.

# 1357 Appendix C

## 1358 **Study of systematic uncertainties 1359 when using cosmics data for 1360 alignment studies**

### 1361 C.1 Residual distribution fit function

1362 The distribution of residuals should be modelled by a double gaussian fit[60]:

$$G(r) = A_s \exp \left[ \frac{-(r - \mu)^2}{2\sigma_s^2} \right] + A_b \exp \left[ \frac{-(r - \mu)^2}{2\sigma_b^2} \right] \quad (\text{C.1})$$

1363 where  $r$  is the residual,  $A$  is the gaussian amplitude,  $\mu$  is the gaussian mean,  $\sigma$  is the  
1364 gaussian sigma, and the subscripts  $s$  and  $b$  stand for signal and background respectively.  
1365 One gaussian captures the real (signal) tracks and the other captures the tracks built from  
1366 noise (background). The gaussian with the smaller width is identified as the signal.

1367 A single gaussian fit failed less often than a double gaussian fit. The gaussian fits were  
1368 performed by initially estimating the amplitude to be 100 tracks, the gaussian mean to be  
1369 the histogram mean, and gaussian  $\sigma$  to be the RMS. The fit range was restricted to  $\pm 1$  RMS  
1370 from the histogram mean. The modification helped the gaussian fit capture the signal peak.  
1371 An example residual distribution is shown in figure C.1.

1372 For all residual distributions in 100 mm by 100 mm bins on layer 4 built from hits on layers 1  
1373 and 2, the difference in gaussian and double gaussian means and  $\sigma$ 's is shown in figure C.2.  
1374 Since the RMS of the residual mean differences distribution is less than 50  $\mu\text{m}$  the gaussian

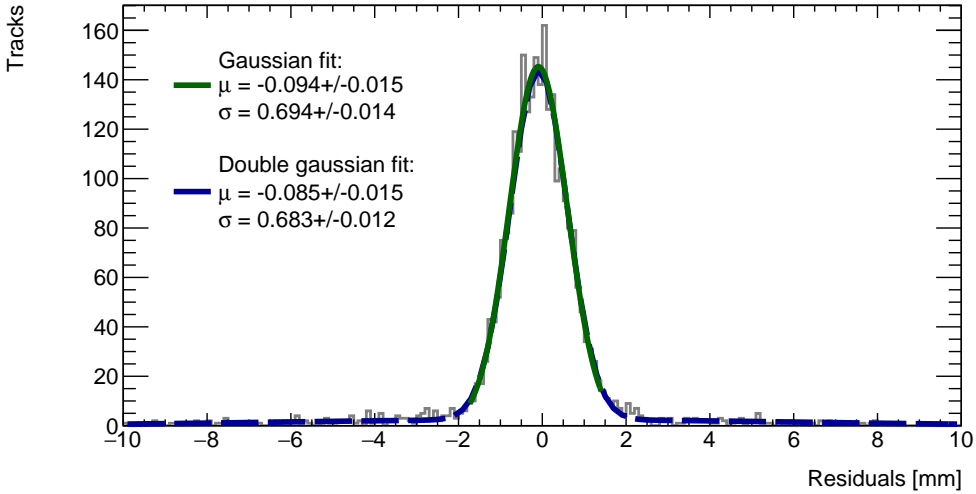


Figure C.1: Residual distribution for tracks on layer 4 built from hits on layers 1 and 2 for  $x \in [-3.00, 97.00]$ ,  $y \in [394.60, 494.60]$  mm for QL2.P.8 fit with a double gaussian and a single gaussian in a range of  $\pm 1$  RMS from the histogram mean.

1375 fit gave the same result within the required precision. Moreover, this is for the tracking  
1376 combination with the worst extrapolation lever arm and the widest distribution of mean  
1377 differences; the interpolation combinations have narrower distributions.

1378 The gaussian  $\sigma$  should be larger than the double gaussian  $\sigma$  because the gaussian distribution  
1379 includes the effect of the noise tracks with large residuals, while the double gaussian models  
1380 signal and background residuals separately. For this analysis, only the residual mean was  
1381 important, so the systematic overestimate of the signal  $\sigma$  in the gaussian fit shown on the  
1382 right of figure C.2 was allowed.

## 1383 C.2 Cosmic muon data collection voltage

1384 Cosmic muon data was collected at 2.9 kV and 3.1 kV because although 2.9 kV is closer to  
1385 the operating conditions the chambers will be subject to in ATLAS, the extra gain provided  
1386 by operating at 3.1 kV increased the signal to noise ratio for pad signals. Also, the tracking  
1387 efficiency was higher with data collected at 3.1 kV. The difference in gain affected the relative  
1388 population of clusters of different sizes, which in turn affected the uncertainty in the strip hit  
1389 positions on each layer, the uncertainty in the track positions and the residual distributions.  
1390 The residual distributions for 3.1 kV data are narrower, as shown in figure C.3.

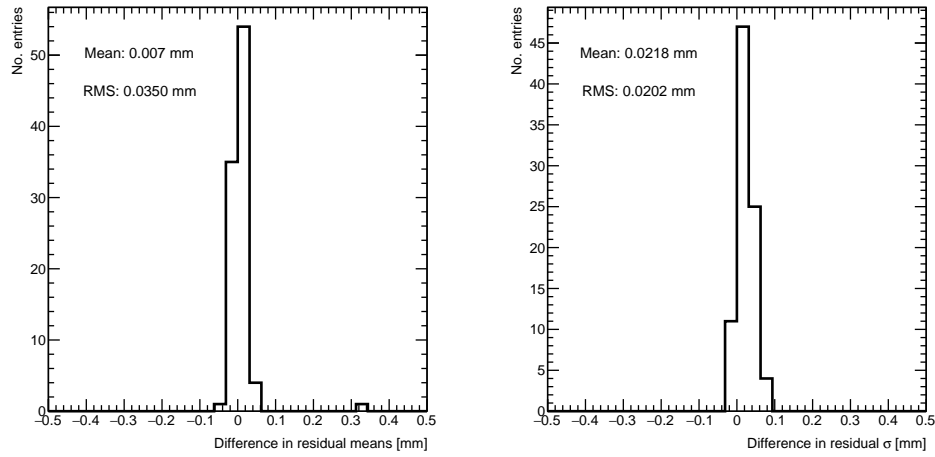


Figure C.2: Difference in residual distribution means and  $\sigma$ 's for a gaussian and double gaussian fit, for all residual distributions in 100 mm by 100 mm bins on layer 4 built from hits on layers 1 and 2 for QL2.P.8.

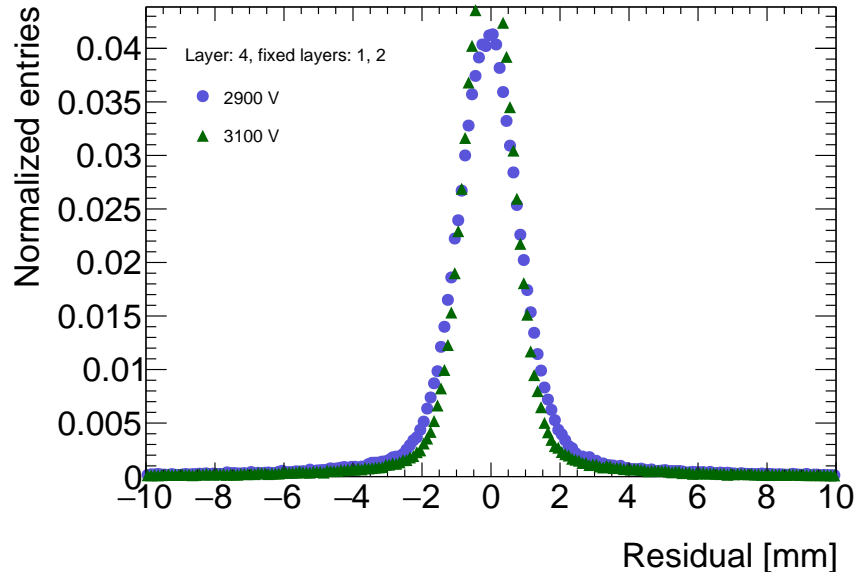
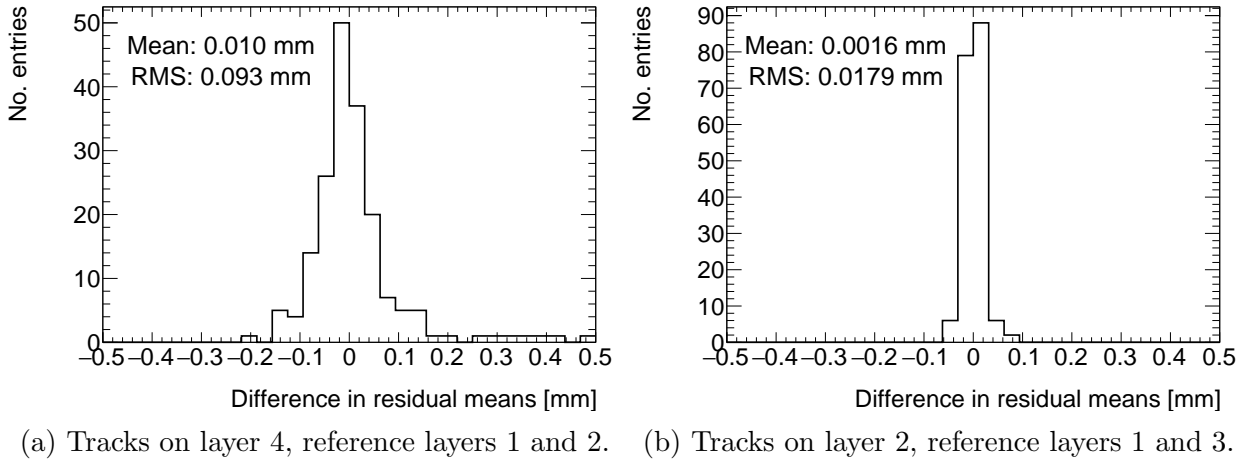


Figure C.3: Residual distribution for tracks on layer 4 built from hits on layers 1 and 2 for QL2.P.8 for data collected at 2.9 kV and 3.1 kV.



(a) Tracks on layer 4, reference layers 1 and 2. (b) Tracks on layer 2, reference layers 1 and 3.

Figure C.4: Difference in residual means for data collected with QL2.P.8 at 2.9 kV and 3.1 kV respectively in 100 mm by 100 mm bins for (a) tracks on layer 4 built from hits on layers 1 and 2 and (b) tracks on layer 2 built from hits on layers 1 and 3.

1391 Neither dataset is better for calculating the mean of residuals in a given area, so a systematic  
 1392 uncertainty can be assigned based on the difference in residual means calculated for 2.9 kV  
 1393 and 3.1 kV data; namely, the systematic uncertainty was approximated as the RMS of the  
 1394 residual mean difference distribution. Data taken with QL2.P.8 was used to estimate the  
 1395 RMS, as in figure C.4a.

1396 Tracks built from hits on layers 1 and 2 and extrapolated to layer 4 have the worst lever arm  
 1397 and hence the most uncertainty. The width of the distribution for geometrically favourable  
 1398 tracks are much narrower. The narrowest width of the residual mean difference distribution  
 1399 is for tracks on layer 2 built from hits on layers 1 and 3 (see figure C.4b).

1400 Therefore, for each tracking combination, a systematic uncertainty equal to the RMS of the  
 1401 residual mean difference distribution was assigned.

### 1402 C.3 Cluster fit algorithm

1403 To ensure that changing the cluster fitting algorithm like in appendix A would not change  
 1404 the calculated mean of residuals in each region of interest significantly, the residual means  
 1405 were compared in both cases. The distribution of the difference in residual means is plotted  
 1406 in figure C.5 for the tracking combination with the worst extrapolation lever arm.

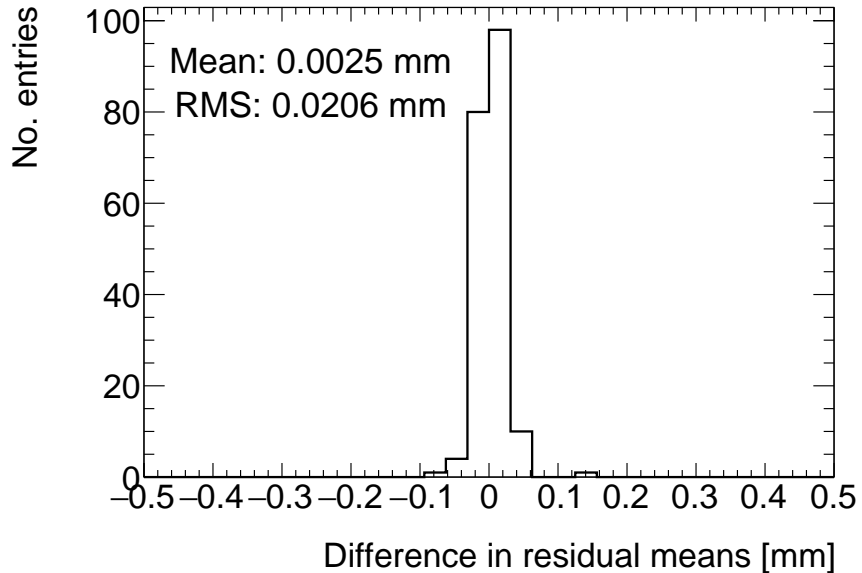


Figure C.5: Difference in residual means when the cluster fit algorithm is `Minuit2` [66] versus Guo’s method [67] for tracks on layer 4 built from hits on layers 1 and 2 for QL2.P.8.

1407 The other tracking combinations had smaller RMS values. Differences on the order of 50  $\mu\text{m}$   
 1408 are important, so figure C.5 shows that the clustering algorithm had a small but notable  
 1409 effect. Therefore, the RMS for each tracking combination will be used to add a systematic  
 1410 uncertainty on the residual means.

## 1411 C.4 Differential non-linearity

### 1412 Definition

1413 In this context, differential non-linearity (DNL) is when the reconstructed cluster mean is  
 1414 biased by the fit of the discretely sampled PDO distribution over the strips. The bias depends  
 1415 on the relative position of the avalanche with respect to the center of the closest strip. For a  
 1416 summary of DNL, refer to page 40 of Lefebvre’s thesis [60] and for an example application,  
 1417 refer to [6].

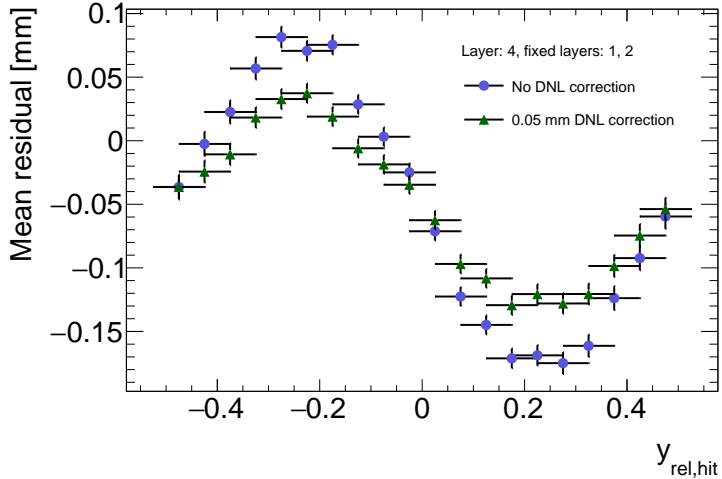


Figure C.6: Effect applying a 50  $\mu\text{m}$  DNL correction to the cluster means on the residual vs  $y_{rel}$  distribution for tracks built from layers 1 and 2 and extrapolated to layer 4 for QL2.P.8.

1418 **Application and effect of DNL**

1419 The cluster mean was corrected for DNL using the equation:

$$y' = y + a \sin(2\pi y_{rel}) \quad (\text{C.2})$$

1420 where  $y$  is the cluster mean,  $y_{rel}$  is the relative position of the cluster mean with respect to  
1421 the strip's center,  $a$  is the amplitude of the correction, and  $y'$  is the corrected cluster mean.  
1422 The amplitude can be derived by comparing the reconstructed hit position to the expected  
1423 hit position, as done in Abusleme, 2016 [6]. With cosmic muons, there is no reference hit  
1424 position to compare to, so track residuals were used as a proxy [60]. The hallmark of the DNL  
1425 effect is the periodic pattern in the residual versus  $y_{rel}$  profile, and the effect of correcting  
1426 the cluster means using an amplitude of 50  $\mu\text{m}$  is shown in figure C.6. An amplitude of  
1427 50  $\mu\text{m}$  was based on Lefebvre's estimate of the DNL amplitudes by layer, quadruplet and  
1428 cluster size using exclusive cosmic muon tracks in `tgc_analysis/CosmicsAnalysis`. Little  
1429 variation was seen in the amplitude parameters with respect to the quadruplet tested, the  
1430 layer and the cluster size so a universal correction was used.

1431 Although the correction is not large enough in this case, the figure shows that the correction  
1432 does reduce the DNL effect. Slightly better performance is seen in the interpolation tracking  
1433 combinations where the quality of the residuals is better. DNL corrections for cosmic muon  
1434 data are difficult because the DNL effect is obscured by the effect of misalignments and

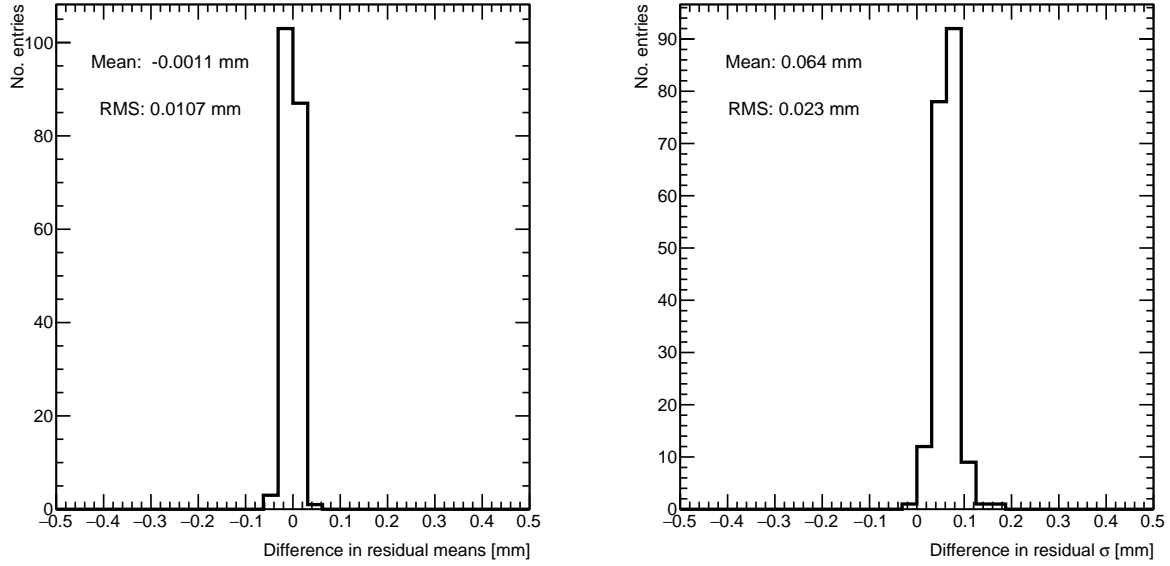


Figure C.7: Difference in residual distribution means and  $\sigma$ 's with and without DNL correction for residuals on layer 4 from reference layers 1 and 2 for QL2.P.8.

1435 noise. Misalignments cause the center of the sine pattern in figure C.6 to be shifted off of  
 1436 zero, since the mean of residuals is shifted.

1437 In figure C.7, it is apparent that the effect of the DNL correction on the mean of the  
 1438 residual distribution in 100 mm by 100 mm areas is on the order of micrometers in the worst  
 1439 extrapolation case. Although the  $\sigma$ 's of the residual distributions shrink with the DNL  
 1440 correction, the mean is the parameter of interest. Therefore, for this analysis DNL was not  
 1441 corrected for.

1442 The  $\sigma$ 's of the residual distributions do shrink with the DNL correction but not so much to  
 1443 affect the residual means, which are the important parameter for this analysis. Therefore,  
 1444 since the effect of the DNL correction is negligible, it was not pursued further.

<sub>1445</sub> Appendix D

<sub>1446</sub> Printable plots

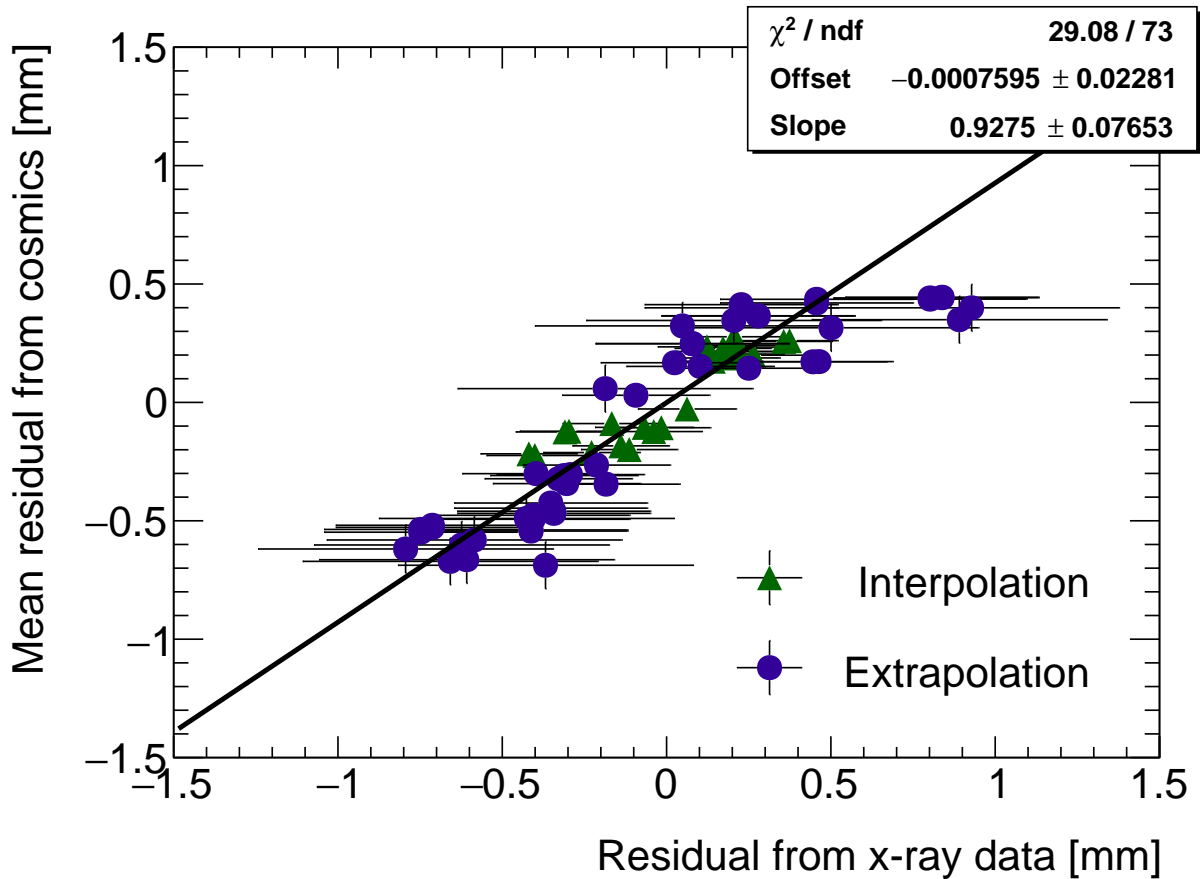


Figure D.1: Correlation plot between x-ray and cosmics residuals for all tracking combinations for QL2.P.11. Each rectangle is centered on an x-ray and mean cosmics residual pair. The width of the rectangles in  $x$  and  $y$  are the uncertainty in the x-ray and mean cosmics residual respectively. This is a printable version of figure 7.2 in section 7.1.

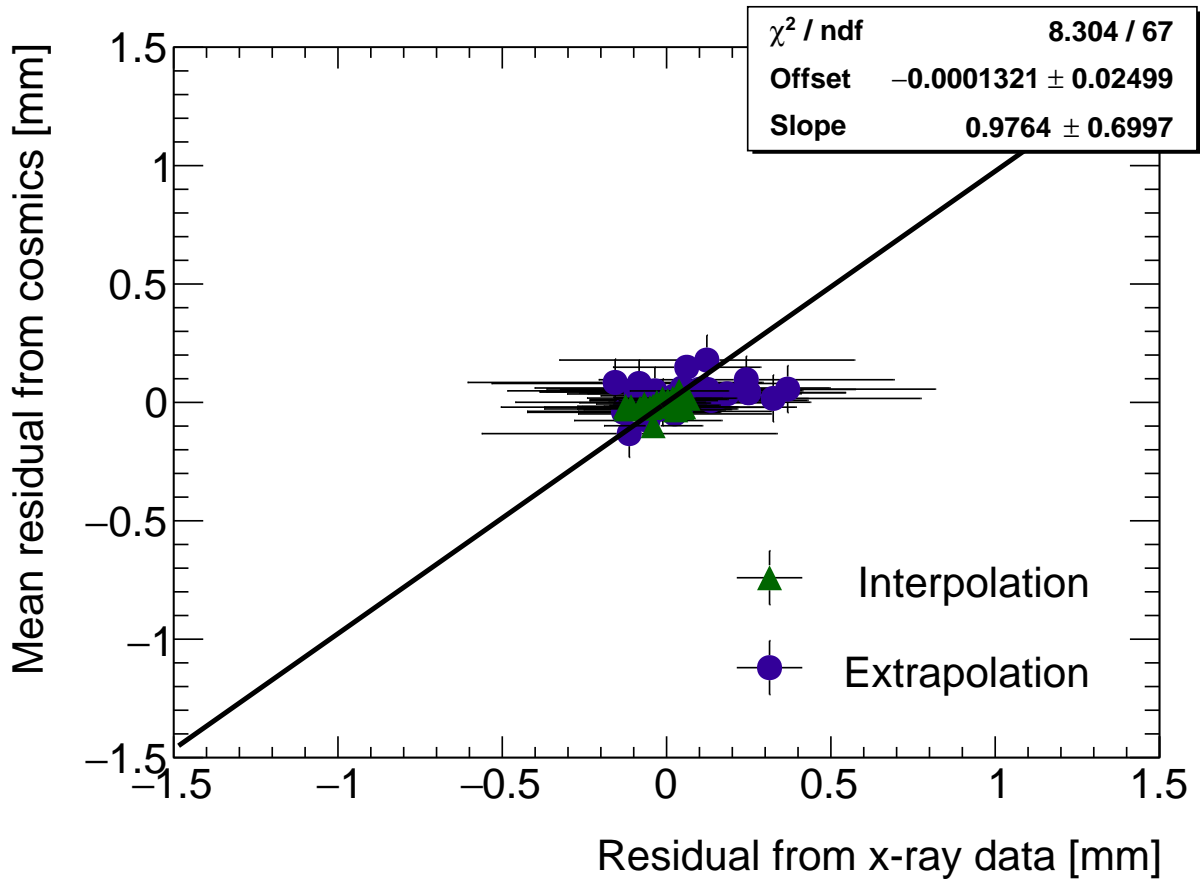


Figure D.2: Correlation plot between x-ray and cosmics residuals for all tracking combinations for QL2.P.8. Each rectangle is centered on an x-ray and mean cosmics residual pair. The width of the rectangles in  $x$  and  $y$  are the uncertainty in the x-ray and mean cosmics residual respectively. This is a printable version of figure 7.3 in section 7.1.